**Ph.D. Research Proposal**

# BOTTOM UP MODULAR CHARACTERIZATION OF SPARSE SPATIAL BIOLOGICAL NETWORKS: APPLICATIONS IN CELL DEATH AND BRAIN VASCULATURE

**by**


**Candidate: Yishaia Zabary**

yishaiaz@post.bgu.ac.il

307963538

**P.I.: Dr. Assaf Zaritsky**

assafzar@gmail.com


PI approval: _____

SISE department chair approval: _____


**Software and Information Systems Engineering Dept.**

**Ben Gurion University**


**November 2022**

# 1. Short Summary – Hebrew

מבנים ותפקודיים רב-תאיים מתאפשרים כתוצאה מאיזון בין רכיבים אינדיבידואליים ומהווים יחדיו את הבסיס לחיים. עד כה, הקשר בין התהוות ורגולציית המבנה הקולקטיבי הגלובלי והפונקציונליות שלו מתוך ההתארגנות ותקשורת בין-תאית הטרוגנית מקומית נותר לא ידוע. התקדמות שדה מחקר זה הוגבלה ע״י קשיים ואתגרים טכניים במדידת התרומה של ההטרוגניות של התאים והמבנים המודולריים המקומיים בזמן ובמרחב, למבנים ולפונקציונליות הביולוגית הגלובליים שנובעים מהם. על מנת לגשר על הפערים הרעיוניים והטכנולוגיים הללו, אני מציע לפתח מסגרת חישובית מוכוונת נתונים, על מנת לאפיין מערכות רב תאיות מורכבות בדמות רשתות, בהן המבנים האטומיים (לדוג׳, תאים) מגדירים את הקודקודים ומחוברים אחד לשני בקשתות. ניתוח של אותן מערכות רב תאיות כרשתות יאפשר כימות ואפיון של הרכיבים המודולריים שמאפשרים ומובילים לפונקציונליות פיזיולוגית ומבנה רקמות שלמות. אדגים גישה זאת באמצעות שתי מערכות של מודלים ניסויים וטכנולוגיות הדמיה שונות: הדמיית מוות תאי קולקטיבי בזמן ובמרחב והדמיה סטטית תלת ממדית במרחב של רשת כלי הדם במוח. במוות תאי קולקטיבי, אחקור את התהליך הדינמי של התפשטות מוות באוכלוסיית תאים, שהוא תוצאה של שילוב בין שני סוגי החלטות של תא בודד - החלטה עצמאית ולא עצמאית (התלויה בסביבה המקומית של התא). בין תוצאותיי הראשוניות, בעזרת שיטות כימות בזמן ובמרחב שפיתחתי, תובנות חדשות על סוג מוות תאי קולקטיבי בשם *פרופטוסיס* (סוג מוות שתלוי בנוכחות מולקולות ברזל). תיאור המוות התאי בעזרת רשת יתבצע באמצעות מידול אירועי מוות של תאים כקודקודים, ומוות קרוב, בזמן ובמרחב, של שני תאים כקשת. ברשת כלי הדם במוח אאפיין את מבני הרשת המקומיים במוח שנגוע בגידולים מסוג *גליובלסטומה* ואמצא את המתאמים בין מיקומי הגידולים, סביבתם המקומית ושל הגרורות שלהם למבני הרשת המקומיים ומצב המחלה. מודל הרשת עצמו יורכב מנקודות פיצולי כלי דם כקודקודים וממקטעי כלי הדם בין הפיצולים כקשתות. בשתי המערכות, אבצע הערכה כמותית של השפעות התפלגות מבנים ודפוסים (בזמן ובמרחב) נשנים ומקומיים (*מוטיפים*), שמהווים את הגורם המקשר בין הרכיב האינדיבידואלי המקומי למבנה הגלובלי והפונקציונליות שלו. כצעד משלים וסופי, אפתח ואפרסם חבילת תוכנה שתאפשר לחוקרים נוספים להשתמש בשיטות אותן פיתחתי.

# 2. Short Summary - English

Multicellular organization and function occurs through complex interplay between many individual cells collectively forming the basis of life. Yet, the fundamental question of how cell heterogeneity and local cell-cell organization and communication principles are integrated to regulate emergent collective structure and function at the global multicellular scale, remains unknown. Progress in this area has been confounded by the technical challenges of accounting for the contribution of cellular heterogeneity and the modular spatial and temporal scales that mediate biological structure and function. I propose to fill these conceptual and technological gaps by developing a data-driven computational framework to model multicellular systems using networks, where the system's "atomic" components (e.g., cells), define vertices that are connected to one another via edges. Network analysis will enable quantitative modeling of the modular components that lead to physiological tissue structure and function. I will demonstrate this approach with two very distinct experimental models and imaging techniques: Live cell imaging of collective cell death and cleared tissue light sheet imaging of brain vasculature. In collective cell death, I will follow the dynamic process of death spreading across a population, that is a consequence of an integration of autonomous and non-autonomous (i.e., environment-dependent) cell death decisions. In preliminary results I developed and applied are new spatiotemporal quantifications to provide more insight on a specific mode of iron-dependent programmed cell death called ferroptosis. The cell death network will be modeled from cells as vertices and close spatiotemporal deaths as edges. In the brain vasculature, I will characterize the structure of the blood vessels network in Glioblastoma brain tumors and correlate the localization of tumor and microenvironment (e.g., immune) cells in relation to local network structures and disease state. The vasculature network will be modeled from bifurcations as vertices and vessels' sections between bifurcations as edges. In both systems I will quantitatively assess the effects of recurring local spatiotemporal patterns (*Motifs*) distributions, which form an intermediate scale of modularity, on global functionalities and mechanisms. Finally, I will develop and release a software that will enable others to use the methods I developed.

## 2.1 Research Plan

Every living organism, from the single cell amoeba to humans, is composed of numerous individual cells that work together to achieve certain functions. Multicellular organisms are built from modular components that cross scales, from a single cell, through a tissue to a full organism (Fig. 2-1, A). In each of these scales, local components interact with one another, and the integration of their local interactions lead to emergent group organization and/or function. Some examples include proper organelle-organelle interactions and organization that are required for proper cell function, and cell-cell interactions that are required for effective collective cell behavior. In my research I am aiming at building the computational infrastructure toward bridging such scales. Specifically, quantitatively characterizing how local interactions between components at one scale (e.g., individual cells) propagate and integrate across time and space toward organization/function at a higher scale (e.g., tissues). Importantly, the traditional approach of perturbing cells and measuring alterations in the collective response cannot explain the bottom-up process of group coordination because population averages mask single cell phenotypic heterogeneity and the spatiotemporal aspects of information across scales. Thus I am taking a different approach of modeling the interactions explicitly as edges in a network, and quantitatively characterizing the network structure and dynamics (when live imaging data is available) to model the emergent collective phenomenon as an integration of local interactions.

The propagation of cell death within a population is one example of an emergent multicellular process. Cell death is a tightly regulated cell function that is critical for proper embryonic development and tissue homeostasis [53], [17], [56]. Dysfunctional regulation of cell death can contribute to the development of degenerative diseases or cancer [96], [77]. While most cell death programs are studied under the premise that a cell's death has no effect on its surrounding neighbor cells, recent studies indicated that cell death can propagate from cell to cell across a population eliminating entire groups [75], [48], [41], [24], [43]. Such collective cell death is observed in various contexts in biology, but the mechanisms underlying it are largely unknown, due in part to a lack of quantitative approaches to systematically follow spatiotemporal death spreading.

The brain vasculature has multiple important physiological functionalities such as transporting oxygen and nutrients across the brain [58], and regulating the movement of ions, molecules, and cells between the blood and the brain (via the blood-brain barrier [44]). Deformation of the brain vasculature can support the growth of Glioblastoma tumors [62], or cause cerebrovascular dysfunction and cognitive impairment [61]. The vasculature's structure is composed of blood vessels that are connected to one another at bifurcations, where blood vessels converge or diverge and proper structure is critical for proper function. The brain vasculature structure is plastic [72], [54] helping the brain to recover from damage, such as adjusting structure and directionality after an ischemic stroke to provide additional blood flow and mitigate the damage [72].

Although these are very different, both of these systems can be computationally modeled as networks, where vertices (single cells / blood vessels and bifurcations) interact with one another locally to form edges (cell-cell death propagation / connecting blood vessels) to eventually form a global structure and function (tissue / brain vasculature) (Fig. 2-1, B). These networks are characterized with strict spatial constraints on the edges (i.e., edges can form only locally) and low ranks (i.e., small number of edges per vertex). This simplification makes these systems attractive toward the challenging goal of quantitative characterization of the transition from local-to-global structure and function.

Each network is constructed from small recurring sub-networks (the local scale), which together compose the entire network (the global scale). Seminal studies established the notion of "network *Motifs*" - recurring sub-networks with defined information processing functions [11]. Motifs detection is a well established methodology to investigate and characterize complex networks [72], [20], [11], [37]. The algorithms used to detect motifs can be partitioned into two major categories and within them, several subcategories: Deterministic motif detection algorithms, where the entire network is traversed and each sub-structure is considered as a motif candidate [21], [13], [8], and probabilistic motif detection algorithms where in each iteration a subnetwork is sampled and examined for motifs candidates [[4], [15], [6], [5]]. All motif detection methods consist of an additional step in which motif candidates are tested for significance to test whether the motif emerges from the network's unique attribute or whether it's a side-effect of the network's basic attributes [21], [31],

all motifs candidates that pass this significance test, are considered as motifs. The same motifs were characterized in transcription networks of multiple experimental systems and organisms suggestive of their role as modular and universal building blocks of transcription networks that are repeatedly selected by evolution for their biological function [20]. Similar motifs also appear in other biological and non-biological networks [14]. I will use known techniques from the field of data science in complex networks (e.g., social networks) and devise novel techniques to adjust for my specific networks' characteristics in order to test the hypothesis that these motifs define a higher layer of abstraction and modularity in multicellular function.

Overall, I hypothesize that in both collective cell death (Chapter 1) and brain vasculature (Chapter 2), the spatial scales are structurally and functionally connected by intermediate scales. In collective cell death, I am developing a method for spatiotemporal quantification of autonomous versus non-autonomous death (Fig. 3-1), measuring the effects of neighboring cell death on a cell's decision to die (under multiple perturbations). I will also model the spread of cell death as a network (Fig. 2-1, B top) in-order to investigate the interplay between local patterns of cell death propagation and global population death patterns. In the brain vasculature, I will develop methodology to characterize network properties at multiple spatial scales and apply it to characterize different brain regions (Fig. 2-1, B, bottom). Once the methodology is established, we will move to a human Glioblastoma (GBM) system, where I will correlate the localization patterns of tumor and the environment cells to local patterns in the vasculature network. Analysis of spatial/spatiotemporal networks will be packaged as easy-to-use software to enable broad applicability across fields (Chapter 3).

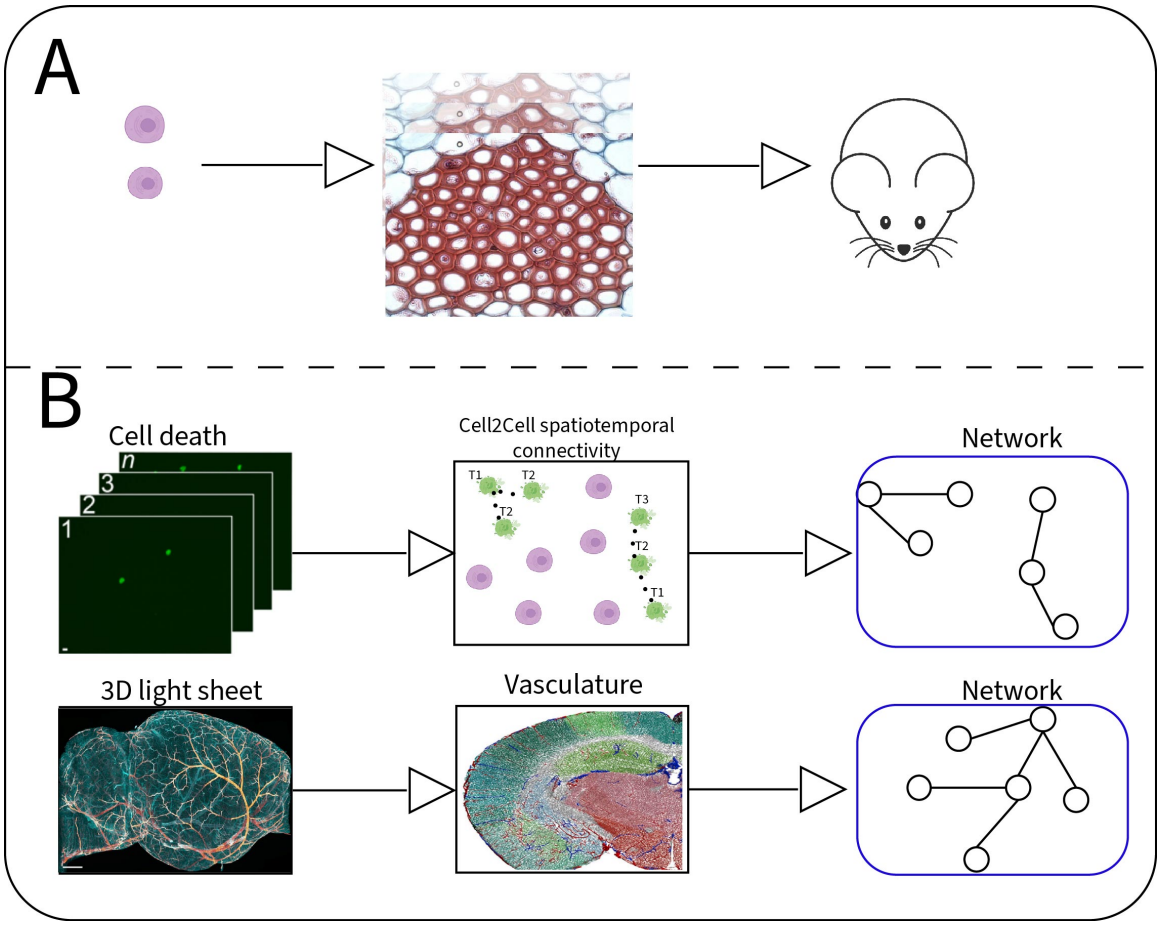


Figure 2-1: (A) Illustration of the hierarchical structure of multicellular organisms. Single cells (left) compose tissues (center) which in turn compose an entire organism (right). (B) Modeling of cell death (top) and brain vasculature (bottom) as a network/graph data structure. Top - the vasculature (middle) itself is segmented from the entire light-sheet 3D scan (left) and modeled as a graph with vessels bifurcations as vertices and vessels as edges (right). Bottom - timelapse of cell death (left) are annotated with each time and location of individual cell deaths (middle), and then modeled as a graph where each cell is a vertex and neighboring (in space and time) cells' deaths are connected by edges.

# 3. Chapter 1 - Spatiotemporal Characterization of Cell Death Spreading

## 3.1 Background and related work

Multiple regulated mechanisms of cell death can occur in metazoan tissues including programs called apoptosis, entosis, necroptosis, pyroptosis, and ferroptosis 21[40]. While the death of an individual cell is typically considered to occur as an isolated, autonomous event, recent observations have shown that the death of individual cells can also have effects on neighboring cells, and in this manner affect entire cell populations [64], [75], [48], [41], [83], [74], [59]. Thus, cell death programs can be characterized as autonomous, where cells die regardless of their environment, and/or non-autonomous, where cell death is influenced by the environment. Cell death through entosis, for example, involves cell killing activity of one cell directed against a neighboring cell [24], [43], [45], [59] Another example is the programmed cell death called Ferroptosis, where a cell is more likely to die if cells around it died recently [75]. Another example of cell non-autonomous death involved apoptotic cells inhibiting death of cells in their vicinity via cell-cell propagation of ERK signaling [87], [98], [84], [46].

The mechanisms underlying the coordination of death on a population scale are largely unknown, due in part to a lack of quantitative approaches to measure the spreading of death across tissues. Moreover, evidence for cell to cell interaction and communication during cell death is progressively accumulating [46], emphasizing the need for methods to quantify the spatial propagation and spread of cell death in a tissue. Current methods quantify the fraction of dead cells in static snapshots or over time [[51], [93]], ignoring the spatial contribution to death spreading. Researchers use the Lag Exponential Death (LED) model [55], [51] to extract the onset and maximum rate of cell death in time and compare it between phenotypes and perturbations. More advanced methods were recently developed to characterize different cell death programs: Measuring the effects of treatments combinations on cell death, termed kinetic modularity profiles [88], which researchers

used to find treatments that accelerated or delayed ferroptosis cell death spreading, and supervised machine learning classification models that automatically distinguish apoptotic from ferroptosis cell death [81]. Although beneficial, these recent methods do not quantify the spread of death in a tissue, and focus either on improving the experimental setup (e.g., mixing treatments or using novel biomarkers [89], [97]), or on a single cell level analysis (e.g., morphological feature extraction [70]) to characterize the behavior of the single cell without taking into account its local environment.

Recently, our lab introduced the Spatial Propagation Index (SPI), a measurement that relies on the difference in death timing of adjacent cell pairs to estimate the likelihood of non-autonomous cell death. SPI was shown to distinguish between autonomous-dominant (apoptosis) and non-autonomous-dominant (ferroptosis) cell death programs [75]. However, SPI does not encode the full complexity of cell death spreading across a population. For example, SPI does not differentiate between a cell that dies surrounded by multiple dead cells, and a cell that dies with only one dead cell in its local environment, as it does not consider the local environment of the cell as a factor. I am proposing a more comprehensive view, in terms of spatiotemporal quantification, of collective cell death. This includes explicit quantification of a cell's autonomous death and of the cells' local environment. My preliminary results demonstrate that these measurements can distinguish between different modes of Ferroptosis and provide more insight regarding mechanism driving cell death spreading across a population.

## 3.2 Data

We are collaborating with Mike Overholtzer from Memorial Sloan Kettering Cancer Center, who is studying mechanisms of cell death. My preliminary results rely on existing data from the Overholtzer lab that were published in [75]. These include time-lapse imaging of ferroptosis, apoptosis and necrosis induced experiments with multiple cell lines and treatments (Tables 3.1, 3.2). The temporal resolution was optimized for each cell type and inducer independently and ranged from 5 to 60 minutes per frame. The raw data was manually annotated, where each cell death event was labeled with its Time of Death (TOD) in minutes after the experiment's first observed cell death.

| Treatment name | Function | Induced cell death program |
|---|---|---|
| C' Dots | Observes iron and distributes it in live cells , causing ferroptosis [35]. | Ferroptosis |
| FAC&BSO | FAC - a combination of 3 cancer chemotherapy medicines. BSO - reduces levels of glutathione and is being investigated as an adjunct with chemotherapy in the treatment of cancer. | Ferroptosis |
| FAC&BSO + PEG1450 | PEG (polyethylene glycols) inhibits rupture of cell membrane (1450 is the molecular weight). | Ferroptosis with inhibited cell rupture |
| FAC&BSO + PEG3350 | PEG inhibits rupture of cell membrane (3350 is the molecular weight). | Ferroptosis with inhibited cell rupture |
| Erastin | Erastin activates voltage-dependent anion channels. Cells treated with erastin are unable to synthesize the antioxidant glutathione. | Ferroptosis |
| ML162 | Disables cells ability to synthesize the antioxidant glutathione | Non propagative ferroptosis [75] |
| superKillerTRAIL | Enhanced ligand with improved stability providing significantly enhanced immune activation. | Apoptosis |
| H2o2 | Oxidizing agent that produces free radicals, leading to oxidative damage to proteins and membrane lipids. | Necrosis |
| TNF+SMAC+zVAD | TNF - leads to pathways to cell survival, differentiation, and proliferation. SMAC - caspase activator shown to promote apoptosis. zVAD- considered as an anti-apoptotic promoter [86]. | Unknown |

Table 3.1: Treatments used. Source: PubChem

| Cell line | Description | Used with treatments |
|---|---|---|
| B16F10 | Melanoma mouse cell line | C' Dots |
| MCF7 | Human breast cancer cell line | FAC&BSO, ML162,H2O2 |
| U937 | Human histiocytic lymphoma cell line | FAC&BSO, TNF+SMAC+zVAD |
| MCF10A | Human non tumorigenic epithelial cell line | FAC&BSO, superkillerTRAIL |
| HAP1 | Cancerous human cell line | FAC&BSO, Erastin, ML162, PEG1450, PEG3350 [75] |

Table 3.2: Cell lines used in experiments

## 3.3 Methods and preliminary results:

### 3.3.1 Differential death spreading dynamics due to altered fraction of autonomous cell death in ferroptosis

Current quantification methods measure cell death spreading without considering the spatial context of the cells' local environment. Our previous measurement of the Spatial Propagation Index (SPI) discriminated between apoptosis and modes of propagating ferroptosis, but was not able to distinguish between different modes of ferroptosis (Fig. 3-1A). SPI quantifies the non-autonomous propagative component in cell death spreading, or to what extent cells are affected by the death of their neighbors. However, SPI misses to quantify the cell autonomous component of spreading, what fraction of the overall death occurs independently of the cells' local environment. Thus, I propose the *Nucleation Index* (and its complementary *Propagation Index*) as a measure for autonomous cell death.

Voronoi tessellation [10] was used to determine the cells' neighbors under a parameterized distance constraint of $\delta$ (Fig. 3-1B, orange bar, in all results $\delta = 50\mu m$). A cell death is considered "autonomous" or "non-autonomous" according to its neighboring cells' death times. More specifically, at each time point, we defined 3 disjointed groups of cells (Fig. 3-1B): (1) Dead cells (green). (2) Nucleation candidates - neighbors to live cells (blue contour). (3) Propagation candidates - neighbors to dead cells (Fig. 3-1B, red contour). When a nucleation candidate dies (Fig. 3-1B, blue dashed contour), we consider its death (termed *nucleation event*) to be *autonomous* and term the cell as a *nucleator*. If a propagation candidate dies (Fig. 3-1B, red dashed contour), we consider its death (termed *propagation event*) to be *Non-autonomous* and term the cell as a *propagator*. The fraction of propagators of the total population of cells is termed the Propagation Index and the fraction of nucleators of the total population is termed the Nucleation Index, both indexes are complementary and amount to 1. It can not be determined that an autonomous death event is truly autonomous and did not occur, for example, from diffusive death factors secreted by other cells. Therefore, the Nucleation Index is a lower bound to the actual fraction of autonomous death in the population, and accordingly, the Propagation Index, is

an upper bound for non-autonomous death. It is important to note that the nucleation index does not correlate to the overall rate of death, as it is indifferent to the magnitude of time passed between cells death. For example, two experiments with different nucleation index scores can have similar, if not identical, rate of death. Consider experiment A, which is characterized with low nucleation index and fast cell to cell death propagation, compared to experiment B, with a nucleation index double the nucleation index of A, but half its cell to cell propagation speed. Intuitively, both characteristics cancel each other out in terms of the overall rate of death difference between A and B.

The SPI and the nucleation index, together, provide a more coherent representation of cell death spreading. SPI provides a quantitative readout for the magnitude in which neighboring cells affect the non-autonomous death decision, going beyond the fraction of non-autonomous cell death measured with the propagation index. While the SPI and the nucleation index are inherently correlated, their 2D landscape shows more information than a pure correlation (Fig. 3-1C). In agreement with [75], apoptosis induction is characterized by high nucleation index and low SPI (Fig. 3-1C, blue contour) while ferroptosis is characterized by low nucleation index and high SPI (Fig. 3-1C, red contour). Interestingly, the nucleation index of non-propagative ferroptosis (ML162 - reported in [75] and shown in Fig. 3-1C, green contours), was characterized with intermediate SPI and nucleation index values compared to apoptosis and propagative ferroptosis. These results suggest that ML162-induced ferroptosis is not entirely a non-propagative mode of ferroptosis.

SPI can not conclusively distinguish between different modes of propagative ferroptosis. Specifically, when examining the subset of fast spreading ferroptosis experiments, those imaged with temporal resolution of at least 15 minutes per frame, we identified that erastin-induced ferroptosis is characterized by a significantly (Mann-Whitney U test [29] with alpha=0.05, p-value<0.0002) smaller fraction of autonomous death compared to other modes of ferroptosis (Fig. 3-1D, red contour).

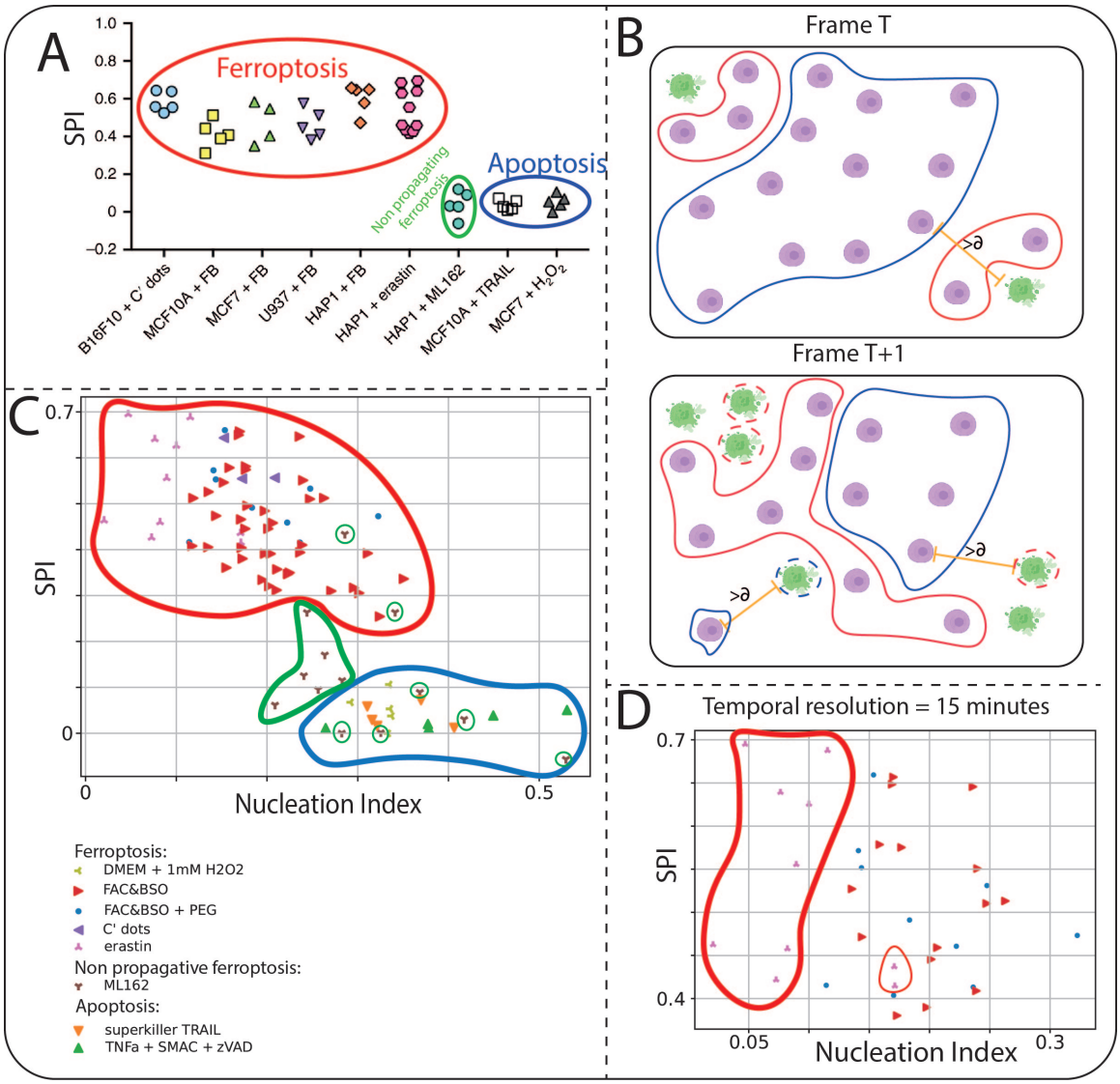


Figure 3-1: (Caption next page.)

### 3.3.2 Quantifying the role of the local environments

SPI and the nucleation index ignore the volume of death, i.e., the numbers of dead cells in a cell's local environment, and the time that passed between neighboring cells' death, hampering our ability to sensitively distinguish between different modes of cell death. For example, consider cell rupture, where the membrane ruptures and the cell bursts, spreading its intracellular content, is upstream of ferroptosis death [65], [50], [68]. We previously showed that ferroptosis occurs through an osmotic mechanism and propagates independently of cell rupture [75]. Specifically, treatment with polyethylene glycols (PEG)

Figure 3-1: Nucleation index - (A) SPI scores of propagating ferroptosis induced experiments (red contour), necrosis and apoptosis induced experiments (blue contour), and non propagative ferroptosis induced experiment (green contour), adapted from [75]. (B) Nucleation and propagation indexes calculation illustration - in time frame T (left), dead cells (green) neighbor, constrained by $\delta = 50\mu m$ distance (Orange bar) cells are considered propagation candidates (red contour) and the rest of the cells, excluding dead cells, are considered nucleation candidates (blue contour). In time frame T+1 (right), each propagation candidate which died (red dashed contour) is considered a propagator and each nucleation candidate that dies (blue dashed contour) is considered a nucleator. (C) SPI about Nucleation Index of ferroptosis, apoptosis and necrosis induced experiments - Each scatter point is an experiment (treatment in legend), mainly non autonomous death with low nucleation index are ferroptosis induced experiments (red contour) and mainly autonomous death with high nucleation index are apoptosis and necrosis induced experiments (blue contour). ML162 experiments, inducing non-propagating ferroptosis death with nucleation index in between nonautonomous and autonomous death experiments scores (green contours). (D) SPI about Nucleation index of ferroptosis induced experiments with a temporal resolution of 15 minutes between frames - Erastin (red contour) is clustered (red contour) separately from the rest of the propagative ferroptosis induced experiments with two outliers. The erastin experiments' nucleation index scores are significantly different from the rest of the treatments' experiments (Mann-Whitney U test [29] with $\alpha = 0.05, p - value < 0.0002$). Scatter markers and colors are identical to the ones in C.

inhibited cell rupture, and reduces the speed by which the death wave propagates through the tissue. However, SPI and the nucleation index were not able to distinguish between PEG-induced to other modes of ferroptosis (Fig. 3-1D, blue dots). To overcome these limitations we propose a more explicit measurement for the environment death state. For a given cell at a given time frame, we recorded the number of dead neighboring cells and the time passed from the most recent death of a neighbor (Delta Time Of Death, $\Delta TOD$). For example, in Fig. 3-2A, the environment death state of the cell marked in orange includes four dead neighbors and 3 time frames since the most recent neighbor's death (cell labeled "dt3"). For each such environment death state, we calculate the probability of a cell to die in the next time frame. These probabilities were normalized in relation to experiment-specific null models derived from 1000 randomized permutations of the same cells' time of death. The Non-Randomality Factor for a given environment death state was defined as the ratio between the simulated and the observed likelihood for cell death (Fig. 3-2A bottom). The more cells' death in a population is composed of autonomous

death, so will the non-randomality factor be closer to 1. Conversely, the more cells' death is nonautonomous, the higher the non-randomality factor will be and further then 1. In general, the higher the non-randomality factor of a specific environment (described by $\Delta TOD$ and the number of dead neighboring cells), the more nonautonomous a cell's decision to die (in that environment). In ferroptosis experiments, where nonautonomous-dominant cell death is the main component, on average, the non-randomality factor decreases with larger values of $\Delta TOD$ and number of dead neighbors because this reflects situations where more cells in the population are dead, the probability of the remaining live cells to die increases, and thus is less dependent in environment death state.

### 3.3.3 Nonautonomous death dominance is indifferent to cell rupture inhibition

The non-randomality factor was calculated for ferroptosis induced experiments with temporal resolutions of 15 minutes between frames, considering an environment of $\Delta TOD$ ranging from 15-75 minutes and 1-5 dead neighbors. Ersatin-induced ferroptosis experiments were characterized with high non-randomality factors, especially for a single dead neighboring cell, providing further support for the dominant role of non-autonomous cell death in ferroptosis (Fig. 3-2B, left). FAC&BSO treatment, which increases the iron peroxide concentration in cells and promotes cell membrane rupture, induces ferroptosis with high non-randomality factor scores similar to Erastin, but smaller in magnitude (Fig. 3-2B, right and center). Although [75] showed that rupture inhibition with PEG in addition to FAC&BSO treatment results in slower propagation of death in the entire tissue, compared to only FAC&BSO induced ferroptosis, PEG treated cells with their rupture inhibited demonstrate similar non-randomality factors scores (Fig. 3-2B, right) to only FAC&BSO treated cells. This suggests that the upstream of propagative death is completely not dependent on cell rupture in the context of the local cell to cell death propagation, but may be dependent in the population scale. My hypothesis is that a cell death rupture releases iron peroxide particles (and perhaps additional ferroptosis inducing substances) to distances further than the cells immediate neighboring cells, the rupture effects will not be captured

by the non-randomality factor, but will increase the overall rate of death. Therefore, density (of the entire population or local crowded clusters of cells) directly relates to the fraction of cells that are hit by cells' inner particles upon rupture, requiring additional experiments perturbed in population global and local densities.

### 3.3.4 ML162 induced ferroptosis propagates in a non-autonomous manner in the short temporal term only

ML162-induced ferroptosis and necrosis induced by H2o2 experiments (Fig. 3-2C). H2o2 experiments' non-randomality factor scores were calculated as a control measurement (Fig. 3-2C, left): If an experiment's non-randomality scores are similar to the H2o2 experiment's score, the experiment can be considered as autonomous death dominant and vice versa. ML162 experiments' non-randomality scores (Fig. 3-2C, right) are higher than H2o2 and show patterns more similar to FAC&BSO and Erastin experiments' scores. Not captured by the nucleation index and SPI, cells treated with ML162 increase their immediate neighbors' probability to die to a limited extent, mostly within the immediate time frame after cell death (Fig. B, right, low $\Delta TOD$ and low number of dead neighbors) and with no apparent accumulation of the death signal (i.e., a single dead neighbor is sufficient to trigger propagating cell death). This shows that ML162 contains a significant, short term and distance, non-autonomous death component, and is not fully non propagative as [75], [81] results suggest. Therefore, ML162 should be more thoroughly examined in terms of non-autonomousity of cell death.

### 3.3.5 Diffusion and not cell to cell communication drive propagation of death in rupture inhibited and non ruptured inhibited ferroptosis

SPI, nucleation index and the non-randomality factor consider the relations between cell death and its immediate neighbors. To investigate the propagation of death beyond the immediate neighbors level, a quantification method which considers the relations between cells and further, more topologically distant cells. By measuring these relations from a distance, the spatial extent of the death signal, caused by each different treatment, can be

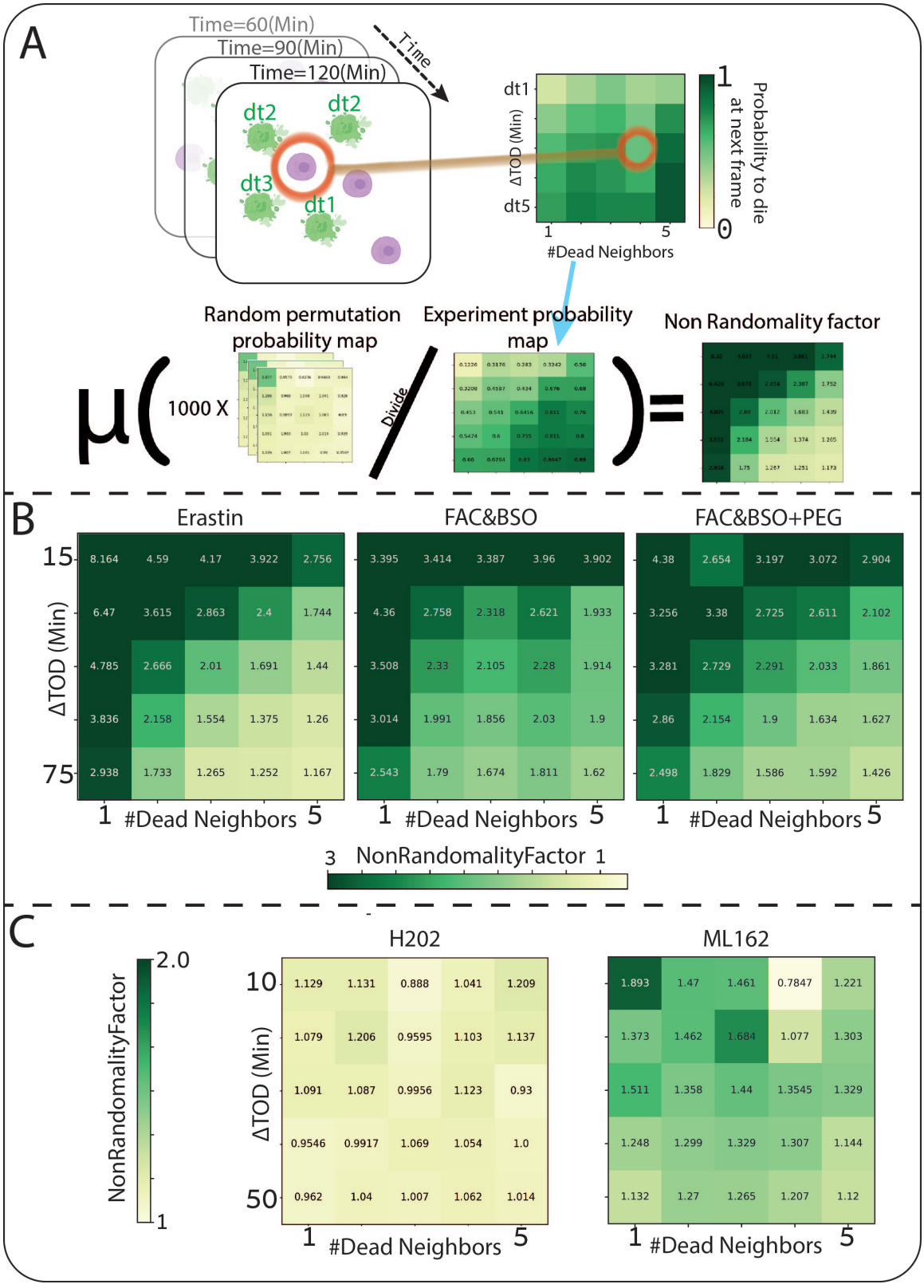


Figure 3-2: (Caption next page.)

Figure 3-2: Non Randomality Factor - (A) Non-randomality factor calculation illustration - in each time frame T, each cell probability to die given a specific environment, characterized by $\Delta TOD$ (the time passed from last neighbor death) and number of dead neighbors, is calculated to form the cell death probability map. Cell i marked in orange contour has 4 dead neighbors with the last one dying dt3 (i.e., 3 time frames) before the current frame. Cell i's probability to die is marked by orange contour on the heatmap. All cell death is randomized (for each experiment separately) 1000 times and the average factor between random death probability maps and the true experimental probability map is the Non Randomality Factor map. (B) Erastin, FAC&BSO and FAC&BSO+PEG induced ferroptosis non-randomality maps of sample experiments - in all propagative ferroptosis experiments the non-randomality factor of cell death increases as the number of neighbors increases and $\Delta TOD$ increases. (C) Non propagative ferroptosis induced by ML162 (right) and necrosis induced by H2o2 (left) non-randomality factor maps - necrosis non-randomality factor map values are all around 1 with a standard deviation of 0.08 suggests completely autonomous death regardless of the number of dead neighbors and $\Delta TOD$ values. ML162 induced non propagative ferroptosis non-randomality factor map values are higher than expected from a non propagative ferroptosis (which should be composed of mainly autonomous death), which suggests that ML162 induced ferroptosis is composed of a larger component of non-autonomous death than expected.

more thoroughly understood. As rupture inhibited cell death (by PEG) induces overall slower rate of death [75] but does not affect local death spreading speed (suggested by our previous results), quantifying the distance by which this observed behavior switches (from fast to slow) is of paramount importance.

Therefore, I propose a method to measure the spatial extent of the effects of cell death on its mid scale environment, termed Death Propagation Spatial Extent. For each cell that dies, termed the *Nucleator cell* (Fig. 3-3A, green cell in Frame 1), 3 disjoint groups of close (in terms of topology and distance) cells are defined as 3 different levels of neighbor cells: (1) L*Layer 1*- cells that are neighbors according to the previously defined neighbors constraint (Fig. 3-3A, blue contour). (2) *Layer 2* - cells that are neighbors to layer 1 cells, excluding other layer 2 cells and the nucleator cell (Fig. 3-3A, green contour), (3), *Layer 3* - cells that are neighbors to layer 2 cells excluding other layer 3 and layer 2 cells (Fig. 3-3A, orange contour). Then, for each frame $T$ (in each experiment), we calculate the overall likelihood of a cell in a given layer to die in the consecutive time frame $T + 1$. For example, in Fig. 3-3A, frame 2, dead cells in the blue contour had a likelihood of 0.4 to die in time frame T. The likelihood averages are then calculated for the entire experiment for each layer,

providing a measurement on the spatial extent that the death signal propagates through the population of cells close to dying cells (but neither local nor global).

The spatial extent of death signal propagation was quantified for each ferroptosis experiment in each time frame and averaged throughout the experiment (Fig. 3-3B). If a the probability to die in a layer of neighbors is higher than another layers' probability, it means that the nucleator cell affected cells in the first layer more than the second. For example, in all ferroptosis experiments, layer number 1 is more affected than layer number 3 and has higher probabilities to die (Fig. 3-2B, top right). Interestingly, it seems that the death signal is not bounded by the immediate topological neighbors (layer 1) of the nucleator cell, as the average probability of a cell from layer 2 to die is larger than the probability of a cell in layer 3 (Fig. 3-3B, bottom left). This suggests that the death signal is not transferred (or communicated) from one cell to another (as a relay race of sorts). This result concedes with the chemical and physical pathway of ferroptosis induced death as it is a cascading death program causing cells to rapture and spread the iron peroxide (which promoted the cell death in the first place) to its environment, regardless of whether cells exist between the affected cells and the initiating cell or an empty space. PEG seems to have no effect on the spatial extent of propagating death, its experiments' cells have increasing probabilities to die the closer they are to the nucleator cell (Fig. 3-4B, red "x"s and purple dashes "-"), similar to cells in other ferroptosis induced experiments. As the nucleator cell and its layers' cells relations are not influenced by the inhibition of cell rupture (by PEG) and have similar probabilities to die as non-rupture-inhibited cells across layers, the hypothesis that cell death's upstream channel is not mainly (or at all) via the membrane rupture and spreading of cell content is further reinforced.

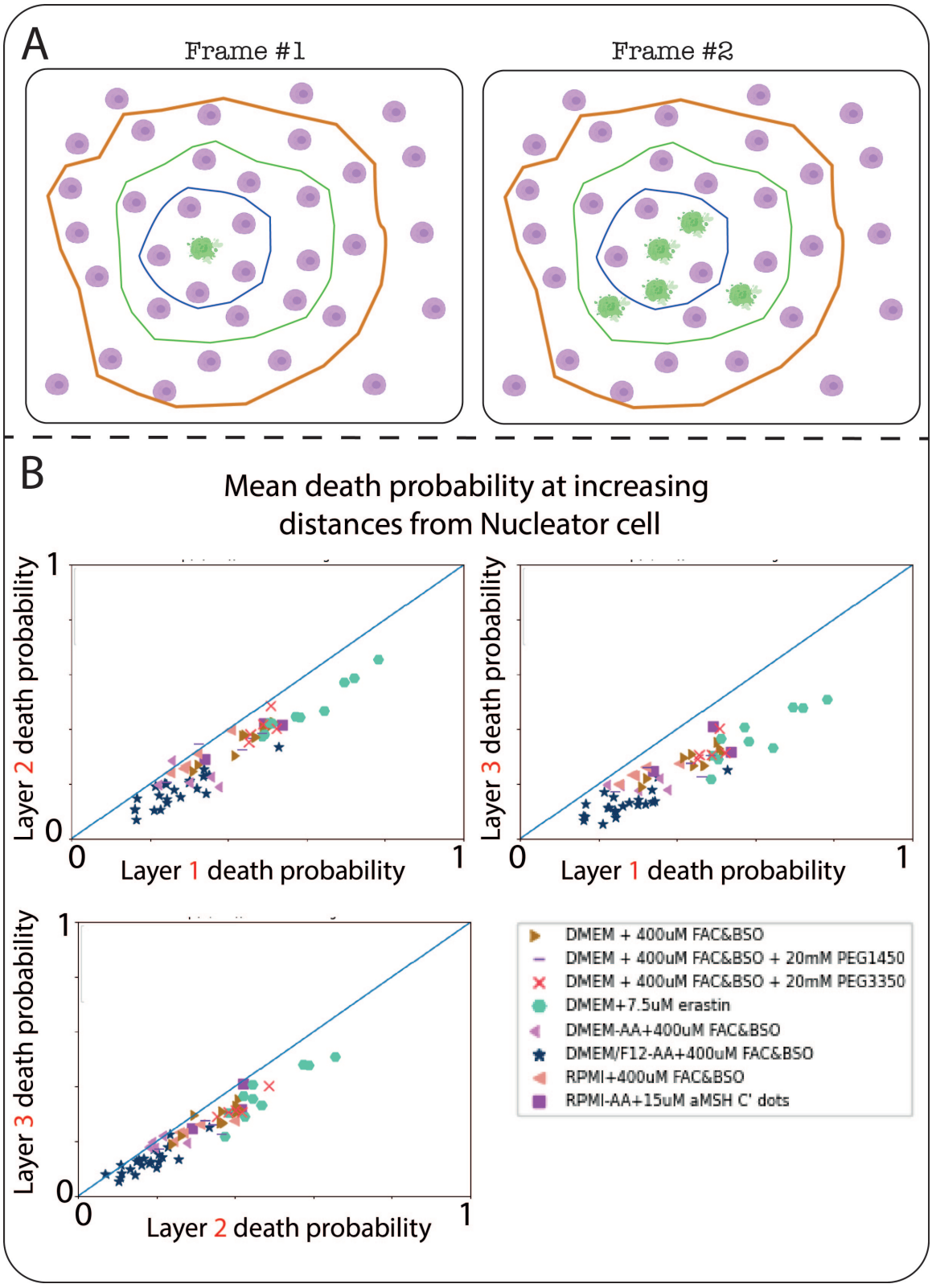


Figure 3-3: (Caption next page.)

Figure 3-3: Death Propagation Spatial Extent - (A) A nucleator cell (green cell in frame #1) mid scale environment is partitioned into 3 disjoint levels of neighbors: level 1 (blue contour), level 2 (green contour) and level 3 (orange contour). The nucleator cell initiates a death wave that propagates to its neighbors. In the next time frame, cells from both layer 1 and 2 die (green cells). (B) Ferroptosis induced experiments - The mean probability of cells to die when part of a level neighbor group of a nucleator cell. Top left - layer 2 cells probability to die about layer 1 cells probability to die, cells at level 1 have a higher likelihood to die in the subsequent frame (of the nucleator death) compared to level 2. Top right - layer 3 cells probability to die about layer 1 cells probability to die, cells at level 1 have a much higher likelihood to die in the subsequent frame compared to level 3, suggesting a decaying diffusion of the propagating death signal. Bottom left - layer 3 cells probability to die about layer 2 cells probability to die, cells at level 2 have a slightly higher likelihood to die in the subsequent frame compared to level 3, suggesting that level 2 neighbors are affected by the nucleator only at the subsequent frame.

## 3.4 Future work

### 3.4.1 Automatic cell death annotation pipeline

Our preliminary research relied on manual death annotations. This is not sustainable with our planned future experiments. Thus, I will develop an automated cell death analysis pipeline. This will rely on cell segmentation and tracking using state of the art software and will be verified by our collaborators by sampling experiments annotations and visually validating their correctness. For the segmentation, tracking and validation, I will use **TrackMate** software package [95] with custom post processing scripts (to convert segmentation annotation to death events annotations).

### 3.4.2 Quantification of density effects on collective cell death

Our preliminary results suggest that diffusion of secreted factors is involved in collective ferroptosis. Diffusion-driven cell death would be more effective in dense cell cultures. Furthermore, recent literature suggests that cell-cell death propagation is influenced by cell-cell adhesions [69], [60], [66], [78]. To systematically assess the relations between cell density and cell death the Overholtzer lab will perform and I will analyze a set of experiments with 10%, 25%, 50%, 75%, and 100% confluency: Erastin will be used to induce ferroptosis, as its nucleation index scores suggest low nucleation rates coupled with fast propagation of cell to cell death signal. PEG will be used with FAC&BSO to measure the effects of population densities on the interplay between the overall rate of death (which PEG reduces) and speed of local propagation of death (which PEG does not affect). ML162 ferroptosis induced experiments will be used to validate our hypothesis that the death induced is composed of significant but moderate nonautonomous components, which will be negligible in low densities, and more apparent in higher densities. In all suggested experiments with higher densities, cell-cell adhesions effects on death propagation will be thoroughly investigated, and on which of the developed methods they affect, enabling us to deduce the component in death propagation influenced by cell-cell adhesions. I will also define a local cell density function (to describe a cell's local environment) and quantify cell

death using our previously developed methods in various population densities to test our hypothesis (Fig. 3-4A). These experiments will complete, together with the preliminary results presented above a first manuscript describing our methodology

### 3.4.3 Local cell death classification by spatiotemporal patterns

*In vivo* cell death takes place in a heterogeneous environment, both in terms of cell types and chemical and physical properties (such as proteins, foreign contagins, etc.). Therefore, a specific cell death program (e.g., ferroptosis, necroptosis, apoptosis, etc.) may not be executed by a group of cells without additional death programs occurring simultaneously in the same tissue or even area. If medical treatment which utilizes cell death (e.g., cancer therapy [101], [91], [90] and Alzheimer disease prevention [80], [92], [85]) is to be developed, a tool to distinguish one cell death program from another while in close spatial proximity to one another is necessary. Therefore, together with our collaborators from the Overholtzer lab at the MSKCC institute, experiments with a population of mixed cell death (e.g., ferroptosis, necroptosis and apoptosis all induced in individual cells and then mixing the cells into a single population) will be conducted. As different cell death programs promote death in different spatiotemporal patterns [75], using these patterns to distinguish between cell death programs seems straightforward. As our previous methods do not encode spatial patterns at all, and do not capture the entire complexity of cell death propagation in both space and time, I will transform the propagation of death to a network representation. Networks can encode all spatial and temporal characteristics of the death propagation. For example, $\Delta TOD$ and distance between cells can be embedded as edge attributes, and the number of dead neighbors at the time of death can be embedded as a vertex attribute. I will utilize graph-theory methods to characterize and classify cell death events as associated with one cell death program or another. We will characterize the structure of our existing non-mixed cell death experiments' networks by detecting the networks' most prevalent recurring modular patterns, termed Motifs (Fig. 3-4B, left). Then, detecting the same motifs in the mixture population networks, and assigning each cell with its network motif (Fig. 3-4B, right), will enable the identification of the cell's death program, and

how the mixture of programs affects the homogeneous (in terms of cell death program) cell decision making.

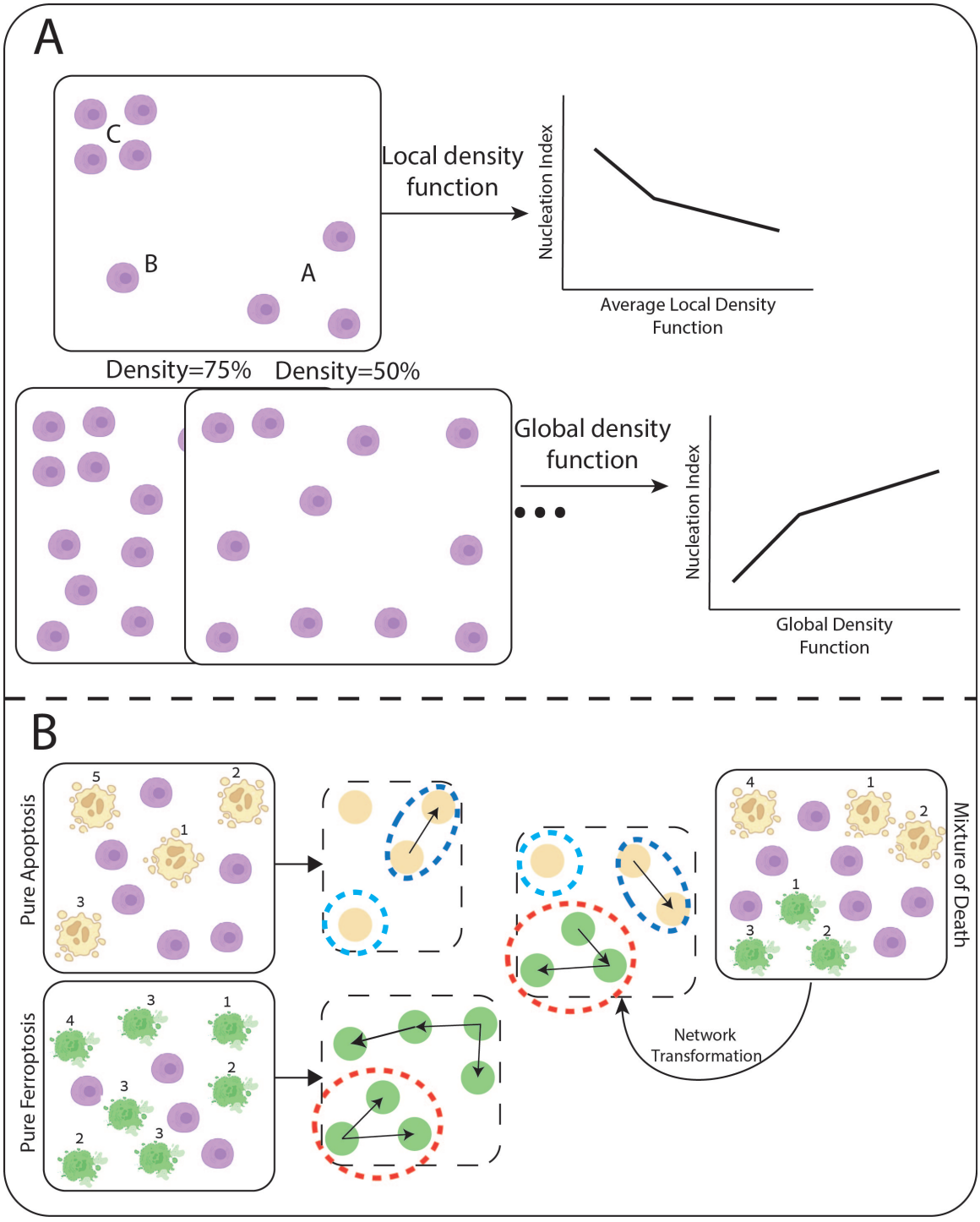


Figure 3-4: Cell death future work - (A) Quantifying local and global density effects on cell death. Top - The average of different local densities (C>A>B) about the experiments Nucleation Index. Bottom - Various global densities experiments about their Nucleation Index. (B) Classification of cell death programs based on the network representation motifs. Motifs from pure apoptosis and ferroptosis networks (Left) are compared to motifs detected in a mixture of cell death networks (Right). Similar motifs (encircled in identical colors) are used to classify the cells' deaths as a specific cell death program.

# 4. Chapter 2 - Brain Vasculature

## 4.1 Background and related work

Blood carries nutrients and cells through the vascular system in the brain. The brain's high metabolic requirements, combined with its low capacity to store energy precipitate the need for a complex and intricate network of arteries, capillaries and veins [16]. Many neurological disorders include a vascular component as part of the core cause or effect of that disorder as previous studies found that even with minimal changes to the regular blood flow, one can compromise the integrity of brain tissue and cause widespread death of neurons [39], [52], [34], [25]. To visualize and measure the structure of the vasculature, recent studies used tissue clearing and 3D light-sheet microscopy and segment its vasculature based on fluorescent marking or staining [12], [94] or immunolabeling [72].

Glioblastoma (GBM), is a rare type of brain tumor, considered to be one of the most challenging malignancies to treat [49]. Patients suffer from poor quality of life, and in most cases, do not survive for long as the tumor spreads [47]. One of the reasons for GBM patients' low survival rate is metastasis spreading via the blood vessels [32], [1]. Therefore, associating vascular structural patterns to localization of tumor and environment cells and to disease prognosis can help detect brain regions that are more prone to developing GBM tumors with potential to personalized medicine.

As brain vasculature is composed of varying scales of size (from microns to several millimeters), all organized in complex patterns, it is very difficult to methodologically study. To that end, many recent studies have focused on methods to map the entire brain vasculature using various techniques, while analyzing the impact of perturbations (such as ischemic strokes, Alzheimer's disease and simple life-style changes) on the vasculature's entire structure and function [67], [94], [18]. However, to our knowledge, only few studies have attempted to investigate the modular components from which the entire vascular network is built from and their organization [72].

## 4.2 Data

We have an ongoing collaboration with Stephane Pages lab from Wyss Center and Nicolas Reiner lab from the Paris Brain Institute Nicolas Reiner lab from the Paris Brain Institute). Our collaborators conducted tissue clearing followed by 3D light sheet microscopy imaging of mice brains under perturbed conditions (such as ischemic stroke and cancer infliction). The 3D imaged brain tissue was processed using the ClearMap2 pipeline [72] and the entire vascular network of the brains was automatically segmented and annotated into a network representation data structure. The network representation is of vessels bifurcations as vertices, and the vessels' sections between bifurcations as edges. The vertices and edges are also described with attributes such as 3D coordinates, whether it is an artery of a vein and others (see tables 4.1 & 4.2). Additionally, for the cancer inflicted brains, we have the coordinates of cancer cells, which were labeled in antibodies to allow detection. Our current data is composed of a single complete mouse brain inflicted by cancer that was used in a previous publication of our collaborators [72] and is available to us. The brain's network consists of inter-connected subnetworks corresponding to >1100 brain regions (annotated by the Allen Institute's Atlas for mice brain regions [26]) and a total of 3,449,637 vertices and 4,896,278 edges. Our data includes 1,273,574 annotated cancer cells with their coordinates and the brain region they are enclosed in according to the Allen Institute Atlas. Ongoing experiments performed by our collaborators are of dissected GBM tumors from human patients which upon completion, will undergo the same processing pipeline and will be available to us as network data structure representations of the vascular network that exists within and around the tumors' tissues.

| Attribute name | Description |
|---|---|
| Coordinates | 3D coordinates (x,y,z) of edge in relation to the axis. Axis 0 point is at the center of the brain tissue in respect to the axis. |
| Radii | The radius of the vessel encoded by the edge in $\mu m$. |
| Artery Binary | A binary variable (True or False), whether the vessel encoded by the edge is an artery or not (meaning vein). |
| Atlas Annotation | The region of the brain the vessel encoded by the edge is part of, according to the Allen institute atlas. |
| Distance to surface | The distance of the vessel encoded by the edge from the surface of the brain (the outermost layer of the brain tissue) in $\mu m$. |
| Length | The length of the vessel encoded by the edge in $\mu m$. |

Table 4.1: Edges attributes in network

| Attribute name | Description |
|---|---|
| coordinates | 3D coordinates (x,y,z) of vertex in relation to the axis. Axis 0 point is at the center of the brain tissue in respect to the axis. |
| Radii | The radius of the vessel's bifurcation encoded by the vertex in $\mu m$. |
| Artery binary | A binary variable (True or False), whether the vessel's bifurcation encoded by the vertex is an artery or not (meaning vein). |
| Atlas annotation | The region of the brain the vessel's bifurcation encoded by the vertex is part of, according to the Allen institute atlas. |
| Distance to surface | The distance of the vessel's bifurcation encoded by the vertex from the surface of the brain (the outermost layer of the brain tissue) in $\mu m$. |

Table 4.2: Vertices attributes in network

## 4.3 Methods and preliminary results

### 4.3.1 Identifying the basic modular components of brain vascular networks

Brain tissue and its vascular network change and adapt to various perturbations to maintain proper function of the brain [38], [72]. Our collaborators previously analyzed the vasculature network in two scales: Global, the change of entire network or subnetworks (of brain regions), and local, which is the change in distributions of recurring submodular components that, when combined together, create the global network. Recent studies measure the global and local scale effects of perturbations on the brain and its vascular network, but do not model the interplay between these scales and how global changes emerge from the small local scale changes [63], [33]. To better understand how the brain vascular network changes and assists the recovery of tissue functionality, and its connection to GBM metastasis, we will identify and quantify the distributions of the underlying modular structures of the vascular system, termed Motifs. Motifs detection is a well established methodology to investigate and characterize complex networks [72], [20], [11], [37]. These motifs are a local structure, and compose the entire vasculature global network, thus bridging the gap between local and global vasculature scales [11]. As a preliminary step, motifs with 4 vertices (K=4) were detected and quantified in 20 different regions of a mouse brain using the ESU and RAND-ESU [19] algorithms. The algorithms were used as implemented in the graph-tool [42] python package. Briefly, the algorithm samples sub-networks from a given graph, and traverses from vertex to vertex to detect and enumerate every motif that is present in that sub-network. Our preliminary results (Fig. 4-1), measured in a cancer inflicted mouse brain, show that motifs have different distributions in different brain regions, suggesting that different motifs serve different functions. In all regions, the star and relay motifs were the most common and the more complex (structurally) motifs had varying distributions (Fig. 4-1). Some motif types appear only in a few regions (Fig. 4-1, the Fasciculus Retroflexus region has no square motifs with crossing edges).

To assess whether detected motifs are a random structure emerging from the basic

characteristics and constraints of the network itself (the target network) or whether they are statistically significant in the specific network, we use a well established method of network randomization and comparison to our target network [30], [2], [28]. We used the edge-swapping algorithm [28] to generate 1000 random networks with the same rank distribution as the target network, and compare the motifs' distributions of the random network to the target network. The motifs significance score was calculated using Z-Score significance test with $\alpha = 0.001$ (Eq. 4.1).

$$Z(Motif) = \frac{f_{input} - \bar{f_{rand}}}{\sigma_{rand}} \tag{4.1}$$

$f_{input}$ is the motif number of appearances in the target network, $\bar{f_{rand}}$ is the motif mean number of appearances in the randomized networks, $\sigma_{rand}$ is the standard deviation of motif appearances numbers in the randomized networks. If $Z(Motif) > 2.0$, the motif is considered statistically significant [37]. The generation of random networks was performed using the random rewiring method with no parallel edges allowed, as implemented in graph-tool python package [42]. Two of the most common motifs (the star shaped motif and the relay, or straight line, motif) have consistently scored a z score of below 2, suggesting that these motifs emerge in completely random networks, and do not represent any unique or significant attribute of the brain region structure (Fig. 4-1, example regions motifs in blue dashed contour). However, more complex motif types do not emerge in substantial numbers in brain regions' networks ($Z - score > 2.0$), and therefore might serve or contribute to a biological functionality of that network and represent an attribute of brain regions network as a whole, and of each specific region (Fig. 4-1, motifs in red dashed contour). To provide a magnitude scale of differences between the motifs' number of occurrences in the target network and in the generated random networks, we calculated the factor between occurrences numbers (Fig. 4-1, green label above each bar). Our preliminary results show two similar regions, in terms of their detected motifs distribution, the Fasciculus Retroflexus and the Cuneiform Nucleus regions that are similar in their number of vertices and edges (Fig. 4-1).

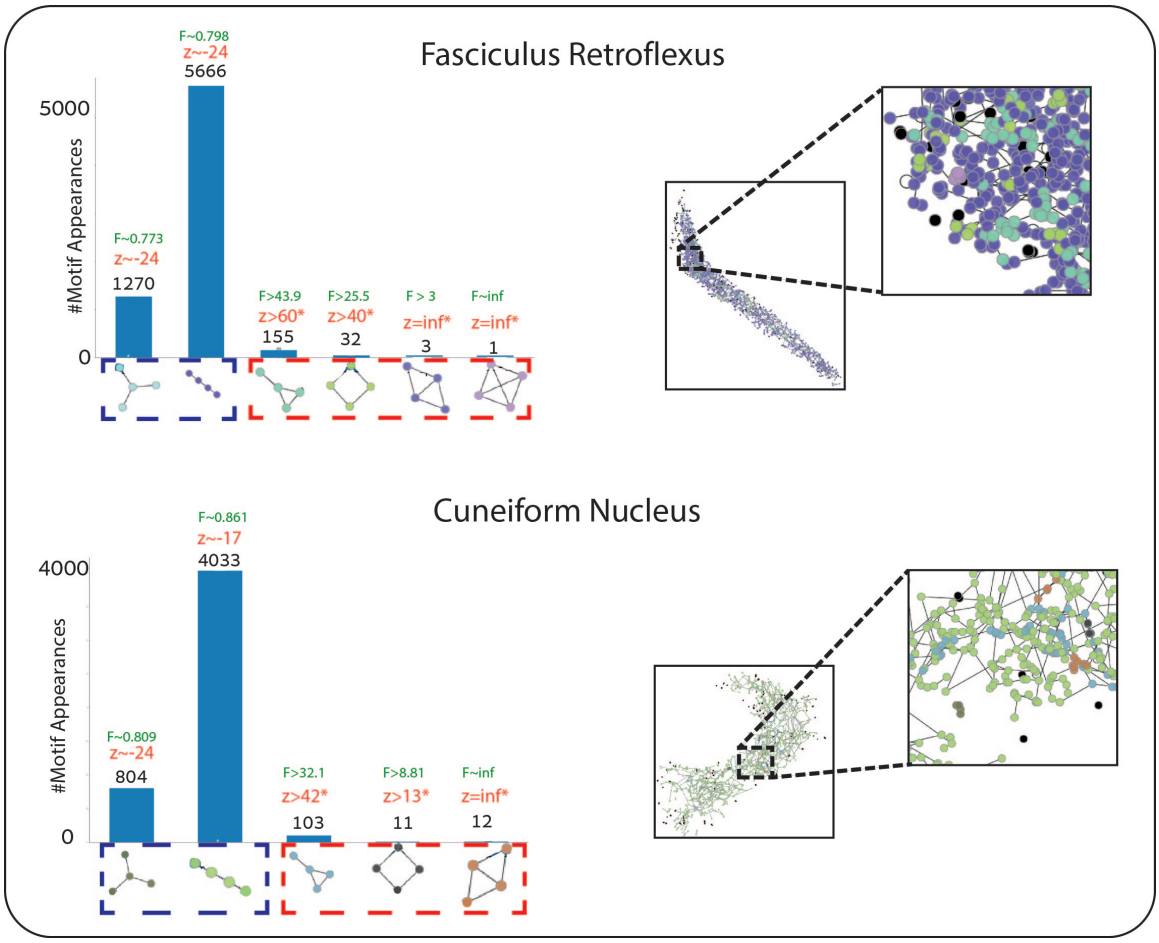


Figure 4-1: Preliminary results of motif distributions in mouse brain regions - Top left, the distributions of motifs in the Fasciculus Retroflexus brain region (2568 #vertices, 2877 #edges). Z-score significance testing scores are in red above each motif type, asterisk marks a significant motif (with $\alpha = 0.001$), $z = \text{inf}$ means no occurrences of that motif has been found in 1000 random networks generated. Factor between motif #occurrences in target network and generated random networks in green ($F = X$). Top right, a visualization of the fasciculus retroflexus network where vertices are color-coded according to the motif they belong to (color of motif as the color of motif in the distribution plot). Bottom left, the distributions of motifs in the Cuneiform Nucleus brain region (#1721 vertices, #1975 edges). Z-score significance testing scores are in red above each motif type, asterisk marks a significant motif (with =0.001), $z = inf$ means no occurrences of that motif has been found in 1000 random networks generated. Factor between motif #occurrences in target network and generated random networks in green ($F = X$). Bottom right, a visualization of the cuneiform nucleus network where vertices are color-coded as the motif they belong to. Red dashed contour marks significant motifs and blue dashed contour marks non-significant motifs.

### 4.3.2 Vascular motifs and cancer cells co-localization

As GBM spreads through the brain tissue using the vascular network [73], it is important to investigate whether GBM cells have preferred types of vessels and vascular structures to traverse through. Here, we propose to use detected motifs' quantification, to map the distributions of motifs, which are a vascular structure representation, about their proximity to GBM cells and tumors. Two example regions, the Striatum and Tectospinal Pathway brain regions, contain 12,713 and 24 #cancer cells (respectively) annotated as within that region. Cancer cells in both the Striatum and the Tectospinal Pathway are more prevalent in proximity to non-significant motifs (Fig. 4-2, motifs in blue dashed contour). However, in the Striatum brain region 148 cancer cells were detected in proximity to significant motifs (Fig. 4-2, motifs in red dashed contour). To complement these distributions, we will map the distributions of vascular structures encompassed within tissues that are mostly composed of GB cells (dissected tumors, future experiments that are currently in progress). Finally, we will develop and train a machine learning model, which will calculate the likelihood for a subsection of a brain vascular network to contain a GB tissue/cells based on its structural attributes.

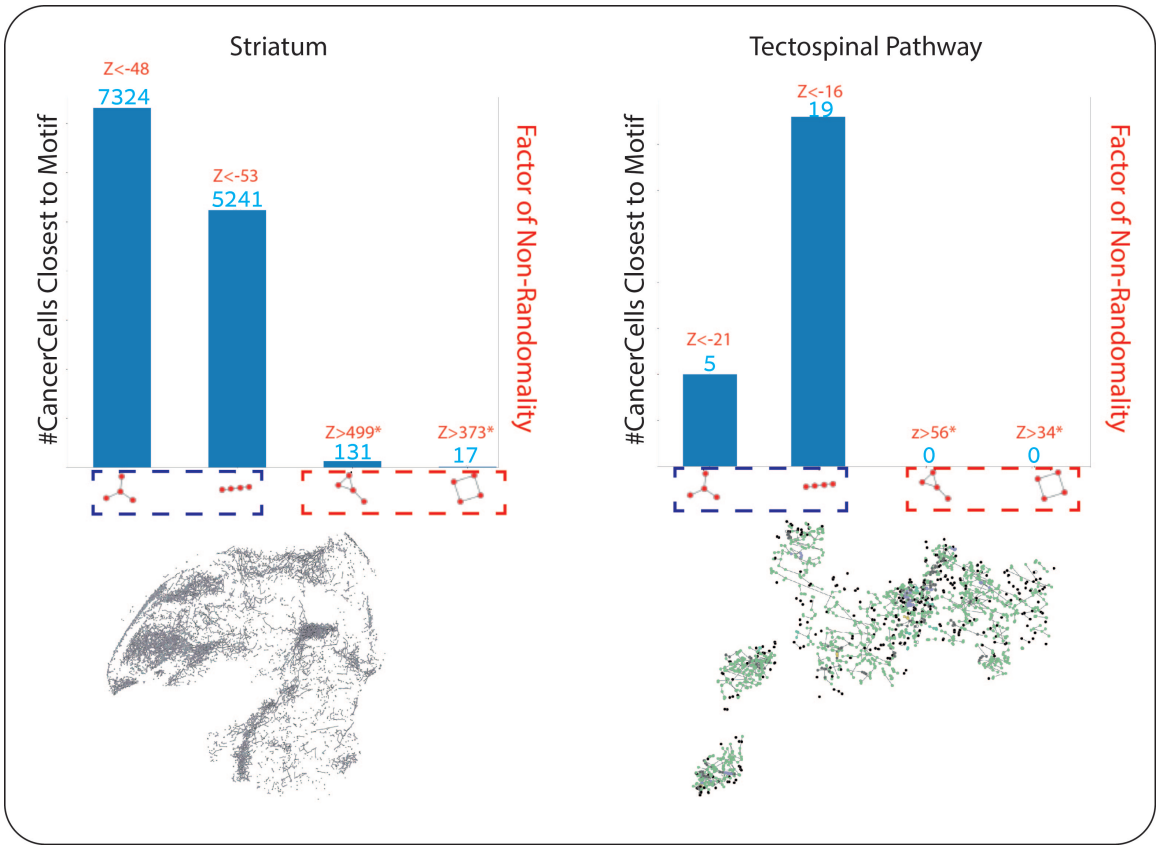


Figure 4-2: Number of cancer cells closest to motif type - A histogram of cancer cell occurrences closest to motifs' types for brain regions, and an illustration of the regions' network below. Regions are the Striatum (17603 vertices, 17965 edges) and Tectospinal Pathway (1867 vertices, 1760 edges) brain regions. Each motif is anointed with its z-significance test score, where asterisk marks a significantly unique motif (with =0.001). The majority of cancer cells in both the Striatum and the Tectospinal pathway are closest to the simple star and relay motifs (left most motifs in each histogram).

## 4.4 Future work

### 4.4.1 Detection of large motifs and classification of motifs functionalities

We intend to expand the common small (<6 vertices) motifs detection efforts [72] to large, more complex detection of motifs in the brain vascular network (>10 #vertices). This will increase the number of possible isomorphic motifs in the network significantly (Fig. 4-3A). To overcome this new constraint, we intend to conjugate several isomorphic motif types into groups, each group representing an estimated biological function. To mitigate the complexity which is hereditary to large motifs' quantification (i.e., the number of possible isomorphic motifs increases exponentially with the motif size constraint, see Fig. 4-3A and Appendix 2: Supplementary methods), we will associate motifs' classes to estimated biological functionalities (Fig. 4-3B), examples include; (1) Motifs with a central vertex, connected by a single edge to all/most other vertices (in its vicinity) can be described as a blood distribution hub, or a star motif (Fig. 4-3B, left). (2) Motifs with a linear structure with a single in and out vertices, termed relays, that can be described as "blood highways", where nutrients can pass in a direct route from one point to another as shortly as possible. This association of biological functionalities of motifs, and the conglomeration of multiple local (in the context of the spatial motif) functionalities into a cohesive global biological effect is differentiated from recent studies which focus on the hierarchical conjunction of local functionalities [79], [79]. This differentiating factor will reveal how simple and explainable motifs (each one with an assigned biological functionality) serve brain functionalities on the local, global and intermediate scales. These estimated biological functionalities will be assessed with our collaborators from the Pages lab, which will provide a biologist's point of view and insights necessary for meaningful partitions. Then, similar motif classes (in terms of their estimated function) will be grouped and labeled as the same function motifs class. Finally, we will map functional motifs classes' distributions to different brain regions and to various regions attributes (region density, region known functionality, etc.).

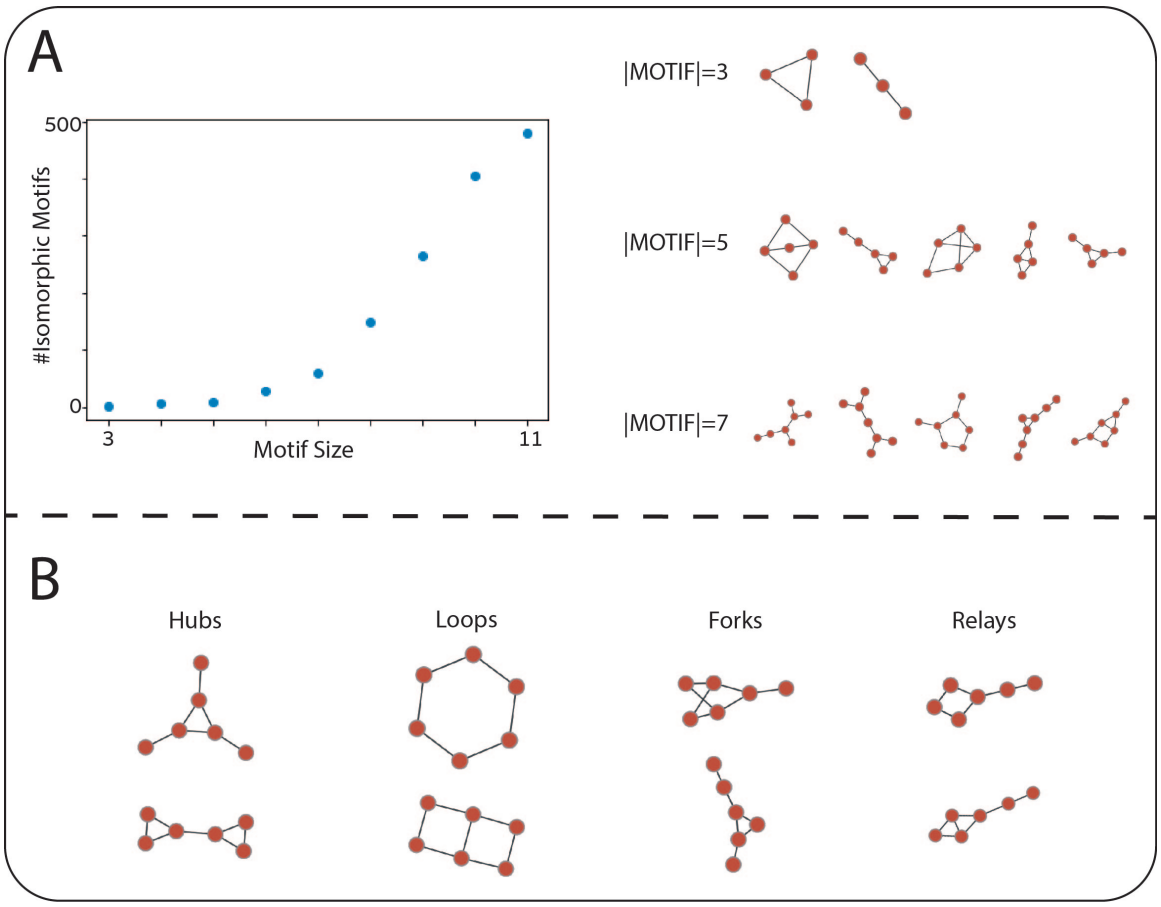


Figure 4-3: Motifs' size effects on complexity and suggested functionalities - (A) Left, the estimated number of non-isomorphic (unique) motifs in a network for increasing motif sizes. Right, examples of motifs with increasing sizes. (B) Examples of possible spatial biological functional motifs.

### 4.4.2 Defining and identifying motifs with anatomical attributes components in brain vascular networks

According to the motifs' isomorphism constraint, two motifs with the same abstract structure are considered as identical and grouped together into a single type (Fig. 4-4, A). This simplifies the representation of the network's motifs and ignores the edges and vertices attributes, such as radii or distance to surface (see tables 4.1 & 4.2), which do not affect the abstract structure. As the brain vascular network includes large variations in attributes values (Fig. 4-4A, shows two isomorphic motifs with substantially different length of the vessel), and as more blood flows through wider and longer vessels, ignoring the different

motifs attributes will not allow for meaningful estimation of the relations between blood vessels and GBM metastasis (as GBM cells traverse via the bloodstream to metastasis). To our knowledge, in the field of network motif detection, no attempts have been made to exacerbate the isomorphism constraints by including edges and vertices' attributes as a distinguishing feature between motif types.

I intend to define an *attribute sensitive* isomorphism function. This function will test for isomorphism between detected motifs using both their abstract structure and their components' (edges and vertices) various attributes. Specifically (and as an initial step), in the brain vascular network, vascular vessels radii and length (see Fig. 4-4A) will be taken into account for the attribute sensitive isomorphism function. We will define *motifs attributable classes* (such as based on vessels' radii, length, artery/vein association etc.) which are significantly different, and quantify their distributions in brain regions and region attributes (similar to subquestion 1). In order to systematically differentiate between vessel attributes (and to establish the significance of difference between motifs attributable classes), we will base our classes on known and established distinct biological categories for each attribute [23]. For instance, in the case of vascular networks and vessels' radii, we will base our significance testing for whether vessel A is of the same attribute class as vessel B on the biological distinction between vessels' types (based on their radii, see Fig. 4-4B). Then, we will associate motifs attributable classes with functional classes and map vessels attributes to biological functions in the context of the entire tissue (i.e., a long, wide vessel might support higher processing requirements of higher-function regions of the brain).

### 4.4.3 Glioblastoma and motifs co-localization in human brain tissue:

As a fundamental part of our investigation into brains' vascular networks, we will obtain datasets of *Glioblastoma* (GBM) inflicted brains and whole dissected tumors, which will be provided by our collaborators from the $\Delta Tissue$ program and our collaborators. This novel dataset will be used to analyze and detect the vascular motifs which characterize GBM infected brain tissue. We will use all of the previously described methods on this data in order to find correlations between GBM cells and motifs. This will enable us to characterize

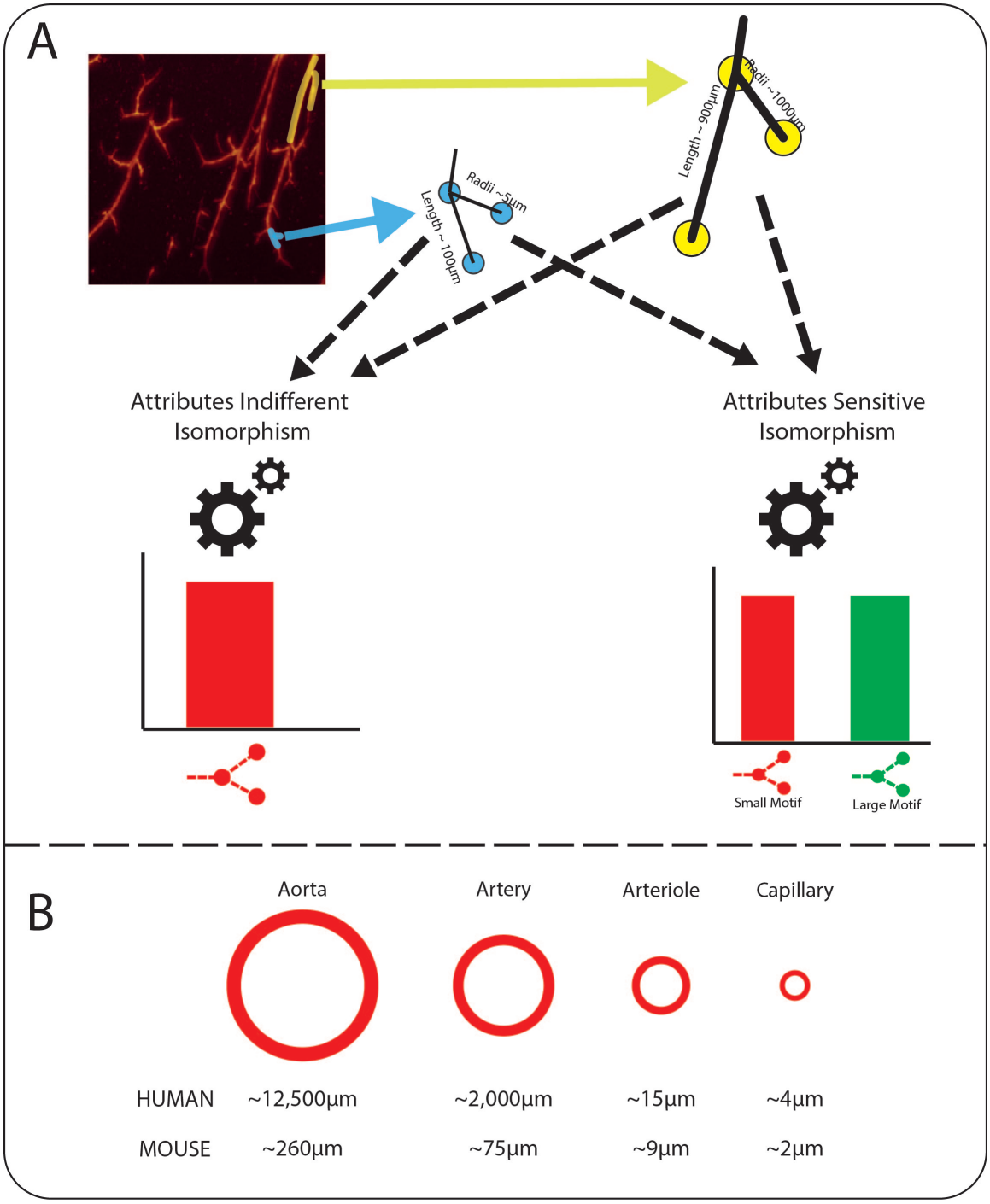


Figure 4-4: Attribute sensitive isomorphism - (A) An illustration of two isomorphic motifs (i.e., attributes indifferent isomorphic) that are significantly different in their attributes. Yellow motif is composed of long arteries, while the blue motif is composed of capillaries. The "Attribute Sensitive Isomorphism" function differentiates between the two motifs (small & large motif in the distribution histogram) while the "Attribute Indifferent Isomorphism" does not. (B) Radii of common vessels in humans and mice.

the most prune regions of the brain to develop GBM tumors and their susceptibility for future metastasis.

# 5. Chapter 3 - Generalized software framework for spatio-temporal analysis of multi-cellular biological networks

## 5.1 Background and related work

A software package to analyze multicellular networks could make the methods developed during my thesis more accessible by others. Many bioimage analysis tools and methods are publicly available. For example, StarDist [57], [76] for cells' segmentation, TrackMate [95] for cell tracking, Napari [99] and Fiji [36] for general purpose visualization and analysis. However, there is no designated software for analysis of spatial networks in the biological domain. General network analysis software include Graph-tool [42] and Neo4J which are designed for large networks (e.g., social networks) analysis by computer scientists and are not suitable for effective use by cell biologists.

## 5.2 Preliminary results: High level design of computational framework

The framework's High Level Design (HLD) goal is to generalize the modeling and analysis of multicellular systems as network data structures (Fig. 5-1A). To this end, two generic approaches are taken: (1) Data conversion - Definition of edges and vertices as described above can be accomplished using HOF design patterns, where the user provides the (simple) software to extract the key events and interactions. (2) Graph analysis - our framework will support multiple graph I/O and analysis engines such as networkX [22], Neo4J, graph-tool [42] and the quick implementation of additional engines. Most importantly, our framework is designed with the goal to allow users to "mix and match" modular parts of known and novel algorithms with ease, e.g., the user will be able to detect motifs using the Kavosh [27] algorithm, while using one of the isomorphism constraint functions we developed such as the attribute sensitive isomorphism function (Fig. 5-1B).

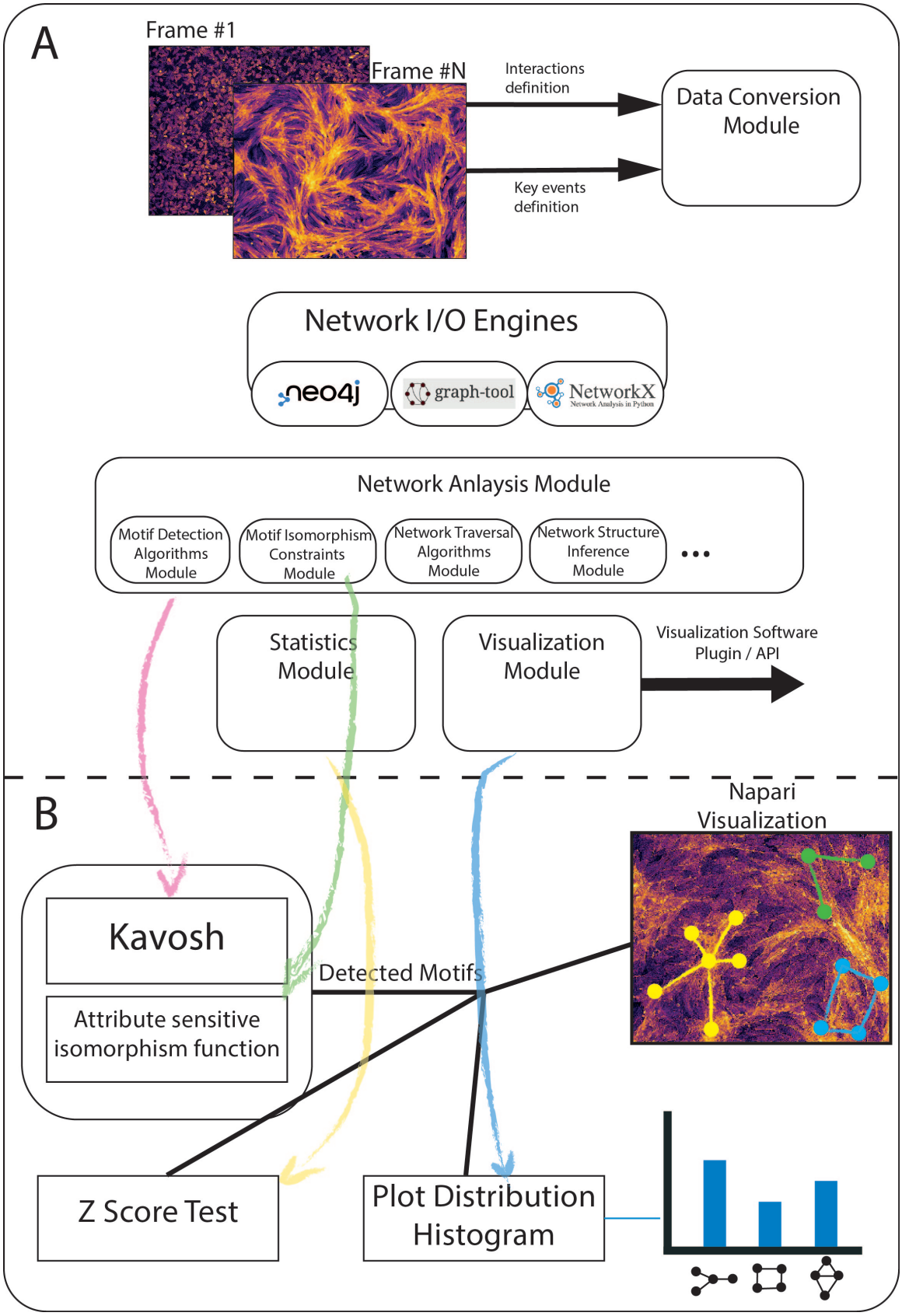


Figure 5-1: (Caption next page.)

Figure 5-1: Framework High Level Design (HLD) and expected user workflow - (A) HLD of the proposed framework, a user provides image based data (temporal or static) and defines the interactions and key events conversion functions. Three network I/O engines are incorporated for existing networks analysis. Main module of network analysis tools contains Motif related algorithms blocks (such as detection and isomorphism definition algorithms), Network & graph traversal algorithms blocks (containing algorithm such as BFS/Ds blocks (containing algorithm such as BFS, Dijkstra, etc.) and additional network analysis components. The framework will also contain a visualization module compatible with other visualization software (such as Napari) and a statistic module to enable statistical significance testing of results. (B) Expected user workflow: The user chooses a combination of algorithms from each required block/module – in the example the user selects the Kavosh algorithm for motif detection but constrained by the Attribute Sensitive Isomorphism (instead of the Kavosh regular isomorphism constraint) and plots the motifs distribution histogram (using our visualization module) while testing for significant difference between motifs distributions in time (using our statistics module). Finally, the user visualizes detected motifs on top of original data using Napari.

## 5.3 Future work

I will expand the software developed during my research to a cohesive end-to-end software framework, providing other researchers with the tools to analyze spatial and spatiotemporal biological networks. To enable easy adaption and use I'll design a generic framework that can be applied to any data following the properties of: (1) ***key events*** (e.g., location and time of cell death) and (2) ***interactions*** (e.g., distance between dying cells or vascular vessels' bifurcations). The corresponding networks will be used as an input to different algorithms . We will integrate into the framework algorithms from the network traversal field, (e.g. BFS [7]) and flow (e.g., max-cut [3]), clustering and graph structure (e.g. cliques detection [9]), as well as the algorithms that will be developed as part of my Ph.D. research. The software will enable efficient comparison between multiple networks. Our framework will be integrated as a plugin to NAPARI [99], enabling computational exploration and visualization.

# 6. Chapter 4 - Other contribution to science

As part of my undergraduate and graduate research in Assaf's lab, I contributed to research projects that do not relate directly to my current proposal.

I developed a new quantification and visualization method to reveal the differential dynamics of early platelets (thrombocytes) spreading, in collaboration with Benny Geiger's lab [71]. Using these tools, we found that platelets sense the substrate on which they adhere and spread using filopodial extensions extruding from the main cell body. We quantified the substrate sensing process by measuring the tapping activity of the platelets extrusions on the substrate and found significant differences in the sensing and spreading mechanisms when platelets are seeded on Collagen IV and Fibrinogen substrates. I also developed a visualization technique to reveal the various states of the platelet during the tapping and sensing process.

I simulated muscle cells (myoblasts) fusion [82], in collaboration with Ori Avinoam's lab. Specifically, I developed a statistical simulation and quantification pipeline which simulates cells' fusion mechanisms in order to verify the team's hypotheses on the factors that are involved in the cells' decision making process and to which other cells they fuse to create a multi-nucleated cell). The pipeline provided statistical inference to verify whether our simulation's results differ from the true behavior observed in in vitro experiments.

I wrote a chapter for the "Bioimage Data Analysis Workflows–Advanced Components and Methods" book, published by Springer Nature [100]. The chapter describes a Matlab based computational pipeline for the quantification of monolayer migration assays which is based on previous software developed in the lab. I restructured the software package and streamlined the user interface while adding several quantification scripts and visualization tools. I also used this computational pipeline to contribute to a manuscript entitled "Dissecting the connection between metastatic phenotypes and Telomerase promoter mutations" which will be released to biorxivs prior to 2023.

# Bibliography


[1] Archinto P Anzil. "Glioblastoma multiforme with extracranial metastases in the absence of previous craniotomy: case report". In: *Journal of neurosurgery* 33.1 (1970), pp. 88–94.

[2] Paul W. Holland, Kathryn Blackmond Laskey, and Samuel Leinhardt. "Stochastic blockmodels: First steps". In: *Social Networks* 5.2 (1983), pp. 109–137. ISSN: 0378-8733. DOI: https://doi.org/10.1016/0378-8733(83)90021-7. URL: https://www.sciencedirect.com/science/article/pii/0378873383900217.

[3] Alan Bundy and Lincoln Wallen. "Breadth-first search". In: *Catalogue of artificial intelligence tools*. Springer, 1984, pp. 13–13.

[4] Gerald Z. Hertz, III Hartzell George W., and Gary D. Stormo. "Identification of consensus patterns in unaligned DNA sequences known to be functionally related". In: *Bioinformatics* 6.2 (Apr. 1990), pp. 81–92. ISSN: 1367-4803. DOI: 10.1093/bioinformatics/6.2.81. eprint: https://academic.oup.com/bioinformatics/article-pdf/6/2/81/515415/6-2-81.pdf. URL: https://doi.org/10.1093/bioinformatics/6.2.81.

[5] Charles E Lawrence et al. "Detecting subtle sequence signals: a Gibbs sampling strategy for multiple alignment". In: *science* 262.5131 (1993), pp. 208–214.

[6] Timothy L Bailey and Charles Elkan. "Unsupervised learning of multiple motifs in biopolymers using expectation maximization". In: *Machine learning* 21.1 (1995), pp. 51–80.

[7] David R Wood. "An algorithm for finding a maximum clique in a graph". In: *Operations Research Letters* 21.5 (1997), pp. 211–217. ISSN: 0167-6377. DOI: https://doi.org/10.1016/S0167-6377(97)00054-0. URL: https://www.sciencedirect.com/science/article/pii/S0167637797000540.

[8] Jeremy Buhler and Martin Tompa. "Finding motifs using random projections". In: *Proceedings of the fifth annual international conference on Computational biology*. 2001, pp. 69–76.

[9] C.H.Q. Ding et al. “A min-max cut algorithm for graph partitioning and data clustering”. In: *Proceedings 2001 IEEE International Conference on Data Mining*. 2001, pp. 107–114. DOI: 10.1109/ICDM.2001.989507.

[10] Qiang Du and Max Gunzburger. “Grid generation and optimization based on centroidal Voronoi tessellations”. In: *Applied Mathematics and Computation* 133.2 (2002), pp. 591–607. ISSN: 0096-3003. DOI: https://doi.org/10.1016/S0096-3003(01)00260-0. URL: https://www.sciencedirect.com/science/article/pii/S0096300301002600.

[11] Ron Milo et al. “Network motifs: simple building blocks of complex networks”. In: *Science* 298.5594 (2002), pp. 824–827.

[12] Tatsuhiko Ebihara et al. “Synchronized formation and remodeling of postsynaptic densities: long-term visualization of hippocampal neurons expressing postsynaptic density proteins tagged with green fluorescent protein”. In: *Journal of Neuroscience* 23.6 (2003), pp. 2170–2181.

[13] MY Galperin and EV Koonin. *Sequence-EVolution-Function*. 2003.

[14] Ron Milo et al. “Superfamilies of evolved and designed networks”. In: *Science* 303.5663 (2004), pp. 1538–1542.

[15] Thomas A. Down and Tim J. P. Hubbard. “NestedMICA: sensitive inference of over-represented motifs in nucleic acid sequence”. In: *Nucleic Acids Research* 33.5 (Jan. 2005), pp. 1445–1453. ISSN: 0305-1048. DOI: 10.1093/nar/gki282. eprint: https://academic.oup.com/nar/article-pdf/33/5/1445/9486250/gki282.pdf. URL: https://doi.org/10.1093/nar/gki282.

[16] Helene Girouard and Costantino Iadecola. “Neurovascular coupling in the normal brain and in hypertension, stroke, and Alzheimer disease”. In: *Journal of Applied Physiology* 100.1 (2006). PMID: 16357086, pp. 328–335. DOI: 10.1152/japplphysiol.00966.2005. eprint: https://doi.org/10.1152/japplphysiol.00966.2005. URL: https://doi.org/10.1152/japplphysiol.00966.2005.

[17] Peter M. Henson and David A. Hume. “Apoptotic cell removal in development and tissue homeostasis”. In: *Trends in Immunology* 27.5 (2006), pp. 244–250. ISSN: 1471-4906. DOI: https://doi.org/10.1016/j.it.2006.03.005. URL: https://www.sciencedirect.com/science/article/pii/S1471490606000925.

[18] Arthur F. Kramer, Kirk I. Erickson, and Stanley J. Colcombe. “Exercise, cognition, and the aging brain”. In: *Journal of Applied Physiology* 101.4 (2006). PMID: 16778001, pp. 1237–1242. DOI: 10.1152/japplphysiol.00500.2006. eprint: https://doi.org/10.1152/japplphysiol.00500.2006. URL: https://doi.org/10.1152/japplphysiol.00500.2006.

[19] Sebastian Wernicke. “Efficient Detection of Network Motifs”. In: *IEEE/ACM Transactions on Computational Biology and Bioinformatics* 3.4 (2006), pp. 347–359. DOI: 10.1109/TCBB.2006.51.

[20] Uri Alon. “Network motifs: theory and experimental approaches”. In: *Nature Reviews Genetics* 8.6 (2007), pp. 450–461.

[21] Pedro Gabriel Ferreira and Paulo J Azevedo. “Evaluating deterministic motif significance measures in protein databases”. In: *Algorithms for Molecular Biology* 2.1 (2007), pp. 1–20.

[22] Aric Hagberg, Pieter Swart, and Daniel S Chult. *Exploring network structure, dynamics, and function using NetworkX*. Tech. rep. Los Alamos National Lab.(LANL), Los Alamos, NM (United States), 2008.

[23] Bert Müller et al. “High-resolution tomographic imaging of microvessels”. In: *Developments in X-Ray Tomography VI*. Ed. by Stuart R. Stock. Vol. 7078. International Society for Optics and Photonics. SPIE, 2008, 70780B. DOI: 10.1117/12.794157. URL: https://doi.org/10.1117/12.794157.

[24] Michael Overholtzer et al. “A non-apoptotic cell death process, entosis, that occurs by cell-in-cell invasion.” In: *Cancer Research* 68.9_Supplement (2008), pp. 1560–1560.

[25] Berislav V. Zlokovic. “The Blood-Brain Barrier in Health and Chronic Neurodegenerative Disorders”. In: *Neuron* 57.2 (2008), pp. 178–201. ISSN: 0896-6273. DOI: https://doi.org/10.1016/j.neuron.2008.01.003. URL: https://www.sciencedirect.com/science/article/pii/S0896627308000342.

[26] Allan R Jones, Caroline C Overly, and Susan M Sunkin. “The Allen brain atlas: 5 years and beyond”. In: *Nature Reviews Neuroscience* 10.11 (2009), pp. 821–828.

[27] Zahra Razaghi Moghadam Kashani et al. “Kavosh: a new algorithm for finding network motifs”. In: *BMC bioinformatics* 10 (Oct. 2009), p. 318. ISSN: 1471-2105. DOI: 10.1186/1471-2105-10-318. URL: https://europepmc.org/articles/PMC2765973.

[28] Lijie Zhang and Weining Zhang. “Edge Anonymity in Social Network Graphs”. In: *2009 International Conference on Computational Science and Engineering*. Vol. 4. 2009, pp. 1–8. DOI: 10.1109/CSE.2009.310.

[29] Patrick E McKnight and Julius Najab. “Mann-Whitney U Test”. In: *The Corsini encyclopedia of psychology* (2010), pp. 1–1.

[30] Brian Karrer and M. E. J. Newman. “Stochastic blockmodels and community structure in networks”. In: *Phys. Rev. E* 83 (1 Jan. 2011), p. 016107. DOI: 10.1103/PhysRevE.83.016107. URL: https://link.aps.org/doi/10.1103/PhysRevE.83.016107.

[31] Kai Liu, William K Cheung, and Jiming Liu. “Stochastic network motif detection in social media”. In: *2011 IEEE 11th International Conference on Data Mining Workshops*. IEEE. 2011, pp. 949–956.

[32] Melody Lun et al. “The natural history of extracranial metastasis from glioblastoma multiforme”. In: *Journal of neuro-oncology* 105.2 (2011), pp. 261–273.

[33] Sara S Nunes et al. “Vessel arterial-venous plasticity in adult neovascularization”. In: *PloS one* 6.11 (2011), e27332.

[34] Berislav V Zlokovic. “Neurovascular pathways to neurodegeneration in Alzheimer’s disease and other disorders”. In: *Nature Reviews Neuroscience* 12.12 (2011), pp. 723–738.

[35] Scott J Dixon et al. “Ferroptosis: an iron-dependent form of nonapoptotic cell death”. In: *Cell* 149.5 (2012), pp. 1060–1072.

[36] Johannes Schindelin et al. “Fiji: an open-source platform for biological-image analysis”. In: *Nature methods* 9.7 (2012), pp. 676–682.

[37] Elisabeth Wong et al. “Biological network motif detection: principles and practice”. In: *Briefings in bioinformatics* 13.2 (2012), pp. 202–215.

[38] Roa Harb et al. “In Vivo Imaging of Cerebral Microvascular Plasticity from Birth to Death”. In: *Journal of Cerebral Blood Flow & Metabolism* 33.1 (2013). PMID: 23093067, pp. 146–156. DOI: 10.1038/jcbfm.2012.152. eprint: https://doi.org/10.1038/jcbfm.2012.152. URL: https://doi.org/10.1038/jcbfm.2012.152.

[39] Costantino Iadecola. “The Pathobiology of Vascular Dementia”. In: *Neuron* 80.4 (2013), pp. 844–866. ISSN: 0896-6273. DOI: https://doi.org/10.1016/j.neuron.2013.10.008. URL: https://www.sciencedirect.com/science/article/pii/S0896627313009112.

[40] Tom Vanden Berghe et al. “Regulated necrosis: the expanding network of non-apoptotic cell death pathways”. In: *Nature reviews Molecular cell biology* 15.2 (2014), pp. 135–147.

[41] Andreas Linkermann et al. “Synchronized renal tubular cell death involves ferroptosis”. In: *Proceedings of the National Academy of Sciences* 111.47 (2014), pp. 16836–16841.

[42] Tiago P. Peixoto. “The graph-tool python library”. In: *figshare* (2014). DOI: 10.6084/m9.figshare.1164194. URL: http://figshare.com/articles/graph_tool/1164194 (visited on 09/10/2014).

[43] Qiang Sun et al. “Competition between human cells by entosis”. In: *Cell research* 24.11 (2014), pp. 1299–1310.

[44] Richard Daneman and Alexandre Prat. “The blood–brain barrier”. In: *Cold Spring Harbor perspectives in biology* 7.1 (2015), a020412.

[45] H Huang, Z Chen, and Q Sun. “Mammalian cell competitions, cell-in-cell phenomena and their biomedical implications.” In: *Current molecular medicine* 15.9 (2015), pp. 852–860.

[46] Ainhoa Pérez-Garijo and Hermann Steller. “Spreading the word: non-autonomous effects of apoptosis during development, regeneration and disease”. In: *Development* 142.19 (Oct. 2015), pp. 3253–3262. ISSN: 0950-1991. DOI: 10.1242/dev.127878. eprint: https://journals.biologists.com/dev/article-pdf/142/19/3253/1839002/dev127878.pdf. URL: https://doi.org/10.1242/dev.127878.

[47] Mary Elizabeth Davis. “Glioblastoma: overview of disease and treatment”. In: *Clinical journal of oncology nursing* 20.5 (2016), S2.

[48] Sung Eun Kim et al. “Ultrasmall nanoparticles induce ferroptosis in nutrient-deprived cancer cells and suppress tumour growth”. In: *Nature nanotechnology* 11.11 (2016), pp. 977–985.

[49] Brian M. Alexander and Timothy F. Cloughesy. “Adult Glioblastoma”. In: *Journal of Clinical Oncology* 35.21 (2017). PMID: 28640706, pp. 2402–2409. DOI: 10.1200/JCO.2017.73.0119. eprint: https://doi.org/10.1200/JCO.2017.73.0119. URL: https://doi.org/10.1200/JCO.2017.73.0119.

[50] Scott J Dixon. “Ferroptosis: bug or feature?” In: *Immunological reviews* 277.1 (2017), pp. 150–157.

[51] Giovanni C Forcina et al. “Systematic quantification of population cell death kinetics in mammalian cells”. In: *Cell systems* 4.6 (2017), pp. 600–610.

[52] Kassandra Kisler et al. “Cerebral blood flow regulation and neurovascular dysfunction in Alzheimer disease”. In: *Nature Reviews Neuroscience* 18.7 (2017), pp. 419–434.

[53] Vangelis Kondylis et al. “The interplay of IKK, NF-$\kappa$B and RIPK 1 signaling in the regulation of cell death, tissue homeostasis and inflammation”. In: *Immunological reviews* 277.1 (2017), pp. 113–127.

[54] Arjang Salehi, John H Zhang, and Andre Obenaus. “Response of the cerebral vasculature following traumatic brain injury”. In: *Journal of Cerebral Blood Flow & Metabolism* 37.7 (2017). PMID: 28378621, pp. 2320–2339. DOI: 10.1177/0271678X17701460. eprint: https://doi.org/10.1177/0271678X17701460. URL: https://doi.org/10.1177/0271678X17701460.

[55] Christian S Backes et al. “Natural killer cells induce distinct modes of cancer cell death: Discrimination, quantification, and modulation of apoptosis, necrosis, and mixed forms”. In: *Journal of Biological Chemistry* 293.42 (2018), pp. 16348–16363.

[56] Vijay A.K. Rathinam and Francis Ka-Ming Chan. “Inflammasome, Inflammation, and Tissue Homeostasis”. In: *Trends in Molecular Medicine* 24.3 (2018), pp. 304–318. ISSN: 1471-4914. DOI: https://doi.org/10.1016/j.molmed.2018.01.004. URL: https://www.sciencedirect.com/science/article/pii/S1471491418300042.

[57] Uwe Schmidt et al. “Cell Detection with Star-Convex Polygons”. In: *Medical Image Computing and Computer Assisted Intervention - MICCAI 2018 - 21st International Conference, Granada, Spain, September 16-20, 2018, Proceedings, Part II*. 2018, pp. 265–273. DOI: 10.1007/978-3-030-00934-2_30.

[58] Melanie D Sweeney et al. “The role of brain vasculature in neurodegenerative disorders”. In: *Nature neuroscience* 21.10 (2018), pp. 1318–1331.

[59] Sarah Bowling, Katerina Lawlor, and Tristan A Rodrıguez. “Cell competition: the winners and losers of fitness selection”. In: *Development* 146.13 (2019), dev167486.

[60] Dean Fennell. *Cancer-cell death ironed out*. 2019.

[61] Abdelrahman Y Fouda, Susan C Fagan, and Adviye Ergul. "Brain vasculature and cognition: Renin-angiotensin system, endothelin, and beyond". In: *Arteriosclerosis, thrombosis, and vascular biology* 39.4 (2019), pp. 593–602.

[62] J Robert Kane. "The role of brain vasculature in glioblastoma". In: *Molecular neurobiology* 56.9 (2019), pp. 6645–6653.

[63] Kim van Kuijk et al. "Heterogeneity and plasticity in healthy and atherosclerotic vasculature explored by single-cell sequencing". In: *Cardiovascular Research* 115.12 (July 2019), pp. 1705–1715. ISSN: 0008-6363. DOI: 10.1093/cvr/cvz185. eprint: https://academic.oup.com/cardiovascres/article-pdf/115/12/1705/31082806/cvz185.pdf. URL: https://doi.org/10.1093/cvr/cvz185.

[64] Michelle Riegman, Michelle S Bradbury, and Michael Overholtzer. "Population dynamics in cell death: mechanisms of propagation". In: *Trends in cancer* 5.9 (2019), pp. 558–568.

[65] Daolin Tang et al. "The molecular machinery of regulated cell death". In: *Cell research* 29.5 (2019), pp. 347–364.

[66] Jiao Wu et al. "Intercellular interaction dictates cancer cell ferroptosis via NF2–YAP signalling". In: *Nature* 572.7769 (2019), pp. 402–406.

[67] Xiaochuan Zhang et al. "High-resolution mapping of brain vasculature and its impairment in the hippocampus of Alzheimer's disease mice". In: *National Science Review* 6.6 (Aug. 2019), pp. 1223–1238. ISSN: 2095-5138. DOI: 10.1093/nsr/nwz124. eprint: https://academic.oup.com/nsr/article-pdf/6/6/1223/38917241/nwz124.pdf. URL: https://doi.org/10.1093/nsr/nwz124.

[68] Aqu Alu et al. "The role of lysosome in regulated necrosis". In: *Acta Pharmaceutica Sinica B* 10.10 (2020). Special Column: Natural Product Screening, pp. 1880–1903. ISSN: 2211-3835. DOI: https://doi.org/10.1016/j.apsb.2020.

07.003. URL: https://www.sciencedirect.com/science/article/pii/S2211383520306298.

[69] Chongshan Dai et al. “Transcription factors in ferroptotic cell death”. In: *Cancer gene therapy* 27.9 (2020), pp. 645–656.

[70] Ayelén Mariana Distéfano et al. “Ferroptosis in plants: triggers, proposed mechanisms, and the role of iron in modulating cell death”. In: *Journal of Experimental Botany* 72.6 (Sept. 2020), pp. 2125–2135. ISSN: 0022-0957. DOI: 10.1093/jxb/eraa425. eprint: https://academic.oup.com/jxb/article-pdf/72/6/2125/36621869/eraa425.pdf. URL: https://doi.org/10.1093/jxb/eraa425.

[71] Melanie B Horev et al. “Differential dynamics of early stages of platelet adhesion and spreading on collagen IV-and fibrinogen-coated surfaces”. In: *F1000Research* 9 (2020).

[72] Christoph Kirst et al. “Mapping the Fine-Scale Organization and Plasticity of the Brain Vasculature”. In: *Cell* 180.4 (2020), 780–795.e25. ISSN: 0092-8674. DOI: https://doi.org/10.1016/j.cell.2020.01.028. URL: https://www.sciencedirect.com/science/article/pii/S0092867420301094.

[73] Tamara T. Lah, Metka Novak, and Barbara Breznik. “Brain malignancies: Glioblastoma and brain metastases”. In: *Seminars in Cancer Biology* 60 (2020). Enigmatic tumor properties associated with metastatic spread, pp. 262–273. ISSN: 1044-579X. DOI: https://doi.org/10.1016/j.semcancer.2019.10.010. URL: https://www.sciencedirect.com/science/article/pii/S1044579X19302275.

[74] Christopher J. Pelham, Masaki Nagane, and Esha Madan. “Cell competition in tumor evolution and heterogeneity: Merging past and present”. In: *Seminars in Cancer Biology* 63 (2020). Emerging role of cell competition in cancer, pp. 11–18. ISSN: 1044-579X. DOI: https://doi.org/10.1016/j.semcancer.2019.07.008. URL: https://www.sciencedirect.com/science/article/pii/S1044579X19300719.

[75] Michelle Riegman et al. “Ferroptosis occurs through an osmotic mechanism and propagates independently of cell rupture”. In: *Nature cell biology* 22.9 (2020), pp. 1042–1048.

[76] Martin Weigert et al. “Star-convex Polyhedra for 3D Object Detection and Segmentation in Microscopy”. In: *The IEEE Winter Conference on Applications of Computer Vision (WACV)*. Mar. 2020. DOI: 10.1109/WACV45572.2020.9093435.

[77] Ying Yang and Daniel J Klionsky. “Autophagy and disease: unanswered questions”. In: *Cell Death & Differentiation* 27.3 (2020), pp. 858–871.

[78] Borong Zhou et al. “Ferroptosis is a type of autophagy-dependent cell death”. In: *Seminars in Cancer Biology* 66 (2020). Autophagic molecules, mediators and modulators in cancer, pp. 89–100. ISSN: 1044-579X. DOI: https://doi.org/10.1016/j.semcancer.2019.03.002. URL: https://www.sciencedirect.com/science/article/pii/S1044579X19300069.

[79] Federico Battiston et al. “The physics of higher-order interactions in complex systems”. In: *Nature Physics* 17.10 (2021), pp. 1093–1098.

[80] Kai Chen et al. “Ferroptosis, a potential therapeutic target in Alzheimer’s disease”. In: *Frontiers in Cell and Developmental Biology* 9 (2021).

[81] Megan Conlon et al. “A compendium of kinetic modulatory profiles identifies ferroptosis regulators”. In: *Nature chemical biology* 17.6 (2021), pp. 665–674.

[82] Tamar Eigler et al. “ERK1/2 inhibition promotes robust myotube growth via CaMKII activation resulting in myoblast-to-myotube fusion”. In: *Developmental Cell* 56.24 (2021), 3349–3363.e6. ISSN: 1534-5807. DOI: https://doi.org/10.1016/j.devcel.2021.11.022. URL: https://www.sciencedirect.com/science/article/pii/S1534580721009461.

[83] Michael R Filbin et al. “Longitudinal proteomic analysis of severe COVID-19 reveals survival-associated signatures, tissue-specific cell death, and cell-cell interactions”. In: *Cell Reports Medicine* 2.5 (2021), p. 100287.

[84] Paolo Armando Gagliardi et al. “Collective ERK/Akt activity waves orchestrate epithelial homeostasis by driving apoptosis-induced survival”. In: *Developmental Cell* 56.12 (2021), 1712–1726.e6. ISSN: 1534-5807. DOI: https://doi.org/10.1016/j.devcel.2021.05.007. URL: https://www.sciencedirect.com/science/article/pii/S1534580721004366.

[85] Md Jakaria et al. “Ferroptosis as a mechanism of neurodegeneration in Alzheimer’s disease”. In: *Journal of neurochemistry* 159.5 (2021), pp. 804–825.

[86] Dan-in Jang et al. “The role of tumor necrosis factor alpha (TNF-$\alpha$) in autoimmune disease and current TNF-$\alpha$ inhibitors in therapeutics”. In: *International journal of molecular sciences* 22.5 (2021), p. 2719.

[87] Takumi Kawaue et al. “Mechanics defines the spatial pattern of compensatory proliferation”. In: *bioRxiv* (2021). DOI: 10.1101/2021.07.04.451019. eprint: https://www.biorxiv.org/content/early/2021/07/05/2021.07.04.451019.full.pdf. URL: https://www.biorxiv.org/content/early/2021/07/05/2021.07.04.451019.

[88] Ryan Richards, Megan E. Honeywell, and Michael J. Lee. “FLICK: An optimized plate reader-based assay to infer cell death kinetics”. In: *STAR Protocols* 2.1 (2021), p. 100327. ISSN: 2666-1667. DOI: https://doi.org/10.1016/j.xpro.2021.100327. URL: https://www.sciencedirect.com/science/article/pii/S2666166721000344.

[89] Sara Francesca Santagostino et al. “Mechanisms of Regulated Cell Death: Current Perspectives”. In: *Veterinary Pathology* 58.4 (2021). PMID: 34039100, pp. 596–623. DOI: 10.1177/0300985821100537. eprint: https://doi.org/10.1177/0300985821100537. URL: https://doi.org/10.1177/0300985821100537.

[90] Dan Wu et al. “Cell death mediated by the pyroptosis pathway with the aid of nanotechnology: prospects for cancer therapy”. In: *Angewandte Chemie* 133.15 (2021), pp. 8096–8112.

[91] Rui Xu et al. “Ferroptosis/pyroptosis dual-inductive combinational anti-cancer therapy achieved by transferrin decorated nanoMOF”. In: *Nanoscale Horizons* 6.4 (2021), pp. 348–356.

[92] Guimei Zhang et al. “The potential role of ferroptosis in Alzheimer’s disease”. In: *Journal of Alzheimer’s Disease* 80.3 (2021), pp. 907–925.

[93] Anabella Aguilera et al. “Do photosynthetic cells communicate with each other during cell death? From cyanobacteria to vascular plants”. In: *Journal of Experimental Botany* (Sept. 2022). erac363. ISSN: 0022-0957. DOI: 10.1093/jxb/erac363. eprint: https://academic.oup.com/jxb/advance-article-pdf/doi/10.1093/jxb/erac363/46673652/erac363.pdf. URL: https://doi.org/10.1093/jxb/erac363.

[94] Hannah C Bennett and Yongsoo Kim. “Advances in studying whole mouse brain vasculature using high-resolution 3D light microscopy imaging”. In: *Neurophotonics* 9.2 (2022), p. 021902.

[95] Dmitry Ershov et al. “TrackMate 7: integrating state-of-the-art segmentation algorithms into tracking pipelines”. In: *Nature Methods* (2022), pp. 1–4.

[96] Douglas R Green. “Cell death and cancer”. In: *Cold Spring Harbor Perspectives in Biology* 14.9 (2022), a041103.

[97] Jenny Jin et al. “Machine Learning Classifies Ferroptosis and Apoptosis Cell Death Modalities with TfR1 Immunostaining”. In: *ACS Chemical Biology* 17.3 (2022). PMID: 35230809, pp. 654–660. DOI: 10.1021/acschembio.1c00953. eprint: https://doi.org/10.1021/acschembio.1c00953. URL: https://doi.org/10.1021/acschembio.1c00953.

[98] Kelvin W Pond et al. “Live-cell imaging in human colonic monolayers reveals ERK waves limit the stem cell compartment to maintain epithelial homeostasis”. In: *eLife* 11 (Sept. 2022). Ed. by Ophir D Klein and Didier YR Stainier, e78837. ISSN: 2050-084X. DOI: 10.7554/eLife.78837. URL: https://doi.org/10.7554/eLife.78837.

[99] Nicholas Sofroniew et al. *napari: a multi-dimensional image viewer for Python*. Version v0.4.17rc8. If you use this software, please cite it using these metadata. Nov. 2022. DOI: 10.5281/zenodo.7276432. URL: https://doi.org/10.5281/zenodo.7276432.

[100] Yishaia Zabary and Assaf Zaritsky. "A MATLAB Pipeline for Spatiotemporal Quantification of Monolayer Cell Migration". In: *Bioimage Data Analysis Workflows–Advanced Components and Methods* (2022), p. 175.

[101] R Xu et al. *Ferroptosis/pyroptosis dual-inductive combinational anti-cancer therapy achieved by transferrin decorated nanoMOF. Nanoscale Horiz. 2021; 6 (4): 348–356. PubMed PMID: 33687417*. Tech. rep. Epub 2021/03/10.